12-2020

A Study on the Triaxial Shear Behavior of Geosynthetic Reinforced Soil by Discrete Element Method

Md Wasif Zaman
The University of Texas Rio Grande Valley

A STUDY ON THE TRIAXIAL SHEAR BEHAVIOR OF GEOSYNTHETIC REINFORCED SOIL BY DISCRETE ELEMENT METHOD

A Thesis

by

Md. Wasif Zaman

Submitted to the Graduate College of
The University of Texas Rio Grande Valley
In partial fulfillment of the requirements for the degree of

MASTER OF SCIENCE

December 2020

Major Subject: Civil Engineering

A STUDY ON THE TRIAXIAL SHEAR BEHAVIOR OF GEOSYNTHETIC REINFORCED SOIL BY DISCRETE ELEMENT METHOD

A Thesis
by
Md. Wasif Zaman

COMMITTEE MEMBERS

Dr. Thang Pham
Chair of Committee

Dr. Thuy Vu
Committee Member

Dr. Jong-Min Kim
Committee Member

December 2020

ABSTRACT

Zaman, Md. Wasif, A Study on The Triaxial Shear Behavior of Geosynthetic Reinforced Soil by Discrete Element Method. Master of Science (MS), December 2020, 79 pp., 5 tables, 24 figures, 132 references.

A 3D DEM model using Particle Flow Code (PFC^{3D}) software was developed utilizing a bonded-ball flexible membrane approach to study cohesionless soil as a discontinuous discrete material. The 3D model was calibrated and verified with experimental data, and a sensitivity analysis was carried out for the microparameters. Triaxial tests were simulated to observe the stress-strain curves and volumetric changes, as well as the strength parameters of soils consisting of spherical particles with different gradations but the same porosity. One important finding is that the relationships between particle size and deviatoric stress, internal friction angle, and dilatancy angle were found to be linear.

Geosynthetics (e.g. geogrid) were added to the developed model to study the stress-strain behaviors of reinforced soil in a geosynthetic reinforced soil (GRS) mass, which have important applications that can improve the design of the structures. Results indicate that geosynthetics improve the cohesion to the granular soil.

DEDICATION

This master's thesis is dedicated to my loving parents, Dr. M. M. Khalequzzaman and Rokeya Zaman, who brought me in this beautiful world and continuously support me in achieving all my goals in life. I am indebted to my loving wife, Asma Akter Moushumi, who has taught me to be optimistic during my difficult time. I sincerely appreciate your love and patience.

ACKNOWLEDGMENTS

I would like to express my heartfelt gratitude to Dr. Thang Pham, chair of this thesis committee who gave me full freedom to conduct this research. Working with Dr. Pham was a lifetime experience that helped me to change my vision to geotechnical engineering.

I would also like to thank Dr. Thuy Vu, a committee member for her thoughtful mentoring and guidance. Dr. Vu was always there to help me writing and preparing a journal article from this research. Besides, I would always be thankful to Dr, Jong-Min Kim for his helping hand towards the completion of this thesis.

I sincerely appreciate the help of Tongming Qu, a Ph.D. student at Swansea University, U.K. for sharing his flexible membrane demo code. Besides I am grateful to Dr. David Potyondy and Mr. Derrick Blanksma from Itasca Consulting Group, Inc. for providing me technical support about the PFC software.

TABLE OF CONTENTS

Page

LIST OF TABLES

Page

LIST OF FIGURES

Page

CHAPTER I

INTRODUCTION

Problem Statement

The strength and strain properties of cohesionless soil which is a granular, discontinuous, and heterogeneous material, are of importance and are usually determined using laboratory tests. Laboratory testing, such as the axisymmetric drained triaxial test, is time-consuming and may require the involvement of highly skilled personnel with expensive instruments. Numerical modeling is another approach to obtaining the cohesionless soil's stress-strain relationship, strength, and volume change. Numerical methods such as the finite element method (FEM) and discrete element method (DEM) have been used for decades to simulate geotechnical laboratory tests to investigate the constitutive laws that apply to this type of soil (Addenbrooke, Potts, and Puzrin 1997; Belheine et al. 2009; Cundall and Hart 1993; Cundall and Strack 1979; Kishino 1988; O'Connor 1996; Sitharam, Dinesh, and Shimizu 2002). For modeling granular materials, FEM, which utilizes continuum mechanical analyses, has some major disadvantages. FEM does not account for the geometry and behavior of a particle as an isolated entity (O'Connor 1996). Moreover, FEM is not capable of modeling physical phenomena such as anisotropy, micro-fractures, and localized instabilities (Belheine et al. 2009). Kishino (1988) stated that the determination of a constitutive model for FEM modeling is significantly difficult (Kishino 1988). With FEM, a constitutive model based on the continuum approach usually requires some

material input or model parameters that sometimes do not have a clear physical meaning. Also, FEM cannot solve the model if the displacement between elements is relatively large since it is formulated by small strain theory. DEM, on the other hand, has better modeling capabilities to capture the mechanicalbehavior of granular material better than FEM does (Cundall and Hart 1993; Sitharam et al. 2002). DEM has also proven to be a reliable approach to delineating the distinct elements that dictate the constitutive behavior of granular materials (Sitharam et al. 2002). DEM can define different particle shapes and sizes: spherical, flaky, elongated, or irregular, small or large. For these advantages, DEM was employed in this study for the analyses of strength and strain properties of cohesionless soil by modeling triaxial testing.

Behaviors of a triaxial test specimen can be significantly affected by the type of confining membrane, especially in terms of reaching peak strength and dilation (Frost and Evans 2009; Henkel and Gilbert 1952; Kuhn 1995; Newland and Allely 1959). Membrane properties significantly affect the movement of particles at the outer edge of a specimen under the application of loads. Vermeer (1990) revealed that the formed shear bands during shear failure are highly dependent on membrane flexibility, i.e., “flexible” or “rigid” (Vermeer 1990). For lab testing, researchers have successfully implemented flexible boundaries to plane strain compression tests (Kozicki and Tejchman 2016; Kuhn 1995; Pham 2009; Powrie et al. 2005; Wang and Yan 2013). The traditional rigid boundary model in DEM analyses has drawbacks compared to the flexible membrane boundary because: (1) a rigid cylindrical wall cannot enable local strain displacement during triaxial shearing, and (2) non-uniform stress distributions exist along the boundary wall due to the forced alignment of particles located near the rigid wall (Bardet and Proubet 1991). Simulated triaxial models with a rigid wall boundary underestimate the deviator stress in the post-elastic zone (Cil and Alshibli 2014; Khoubani and Evans 2018).

With the rigid wall, the actual failure surface and the volume change cannot be determined. The DEM flexible membrane model best reflects the real working condition of a triaxial test, but the modeling approach is complicated and computationally expensive. Nevertheless, because of its advantages, the flexible modeling approach was adopted for this study.

The effects of particle size on the behavior of discontinuous granular materials has generated much research for many years (Bolton 1986; Kim, Sagong, and Lee 2005; Rowe 1962; Seo, Ha, and Kim 2007) with both experiments and modeling. As Ben et al. (2010) and Cundall and Hart (1993) stated, the effects of particle size must be identified to obtain accurate predictions of the behavioral characteristics of granular soil (Ben-David, Rubinstein, and Fineberg 2010; Cundall and Hart 1993). However, studies on the effects of particle size have been somewhat inconsistent and contradictory. Kirkpatric (1965) and Marschi et al. (1972) concluded from experimental studies that the friction angle decreases with increasing uniform particle size (Kirkpatric 1965; Marschi, Chan, and Seed 1972). Xiaofeng et al. (2013) investigated the effect of coarse-grained content on the stress-strain response of gravel soil and concluded that shear strength increases with the increase of coarse gravel content in the specimen (Xiaofeng et al. 2013). Kim and Ha, (2014) performed large direct shear tests and concluded that a larger particle size results in higher shear strength (Kim and Ha 2014). However, Sitharam et al. (2000) with DEM triaxial test simulations observed no significant changes in shear strength and volume change due to particle size for parallel gradations; shear strength decreases to a considerable extent for a wider gradation which results in a decrease in the angle of internal friction (Sitharam and Nimbkar 2000). Bagherzadeh-Khalkhali and Mirghasemi (2009) using a DEM model to simulate direct shear test reported that internal friction angle and dilation increase due to particle size is more significant by scalping gradation than parallel gradation

(Bagherzadeh-Khalkhali and Mirghasemi 2009). Mishra and Mahmud (2017) performed DEM direct shear test simulations to study particle size effects on two commonly used ballast gradations for railroad tracks, Arema #4 and Arema #24 (Mishra and Mahmud 2017). Significant changes in internal friction angle due to particle size were observed for Arema #4 ballast material, however, no consistent trend was found for gradually changing gradation for Arema #24. Islam et al. (2011) performed a series of direct shear tests considering uniform particles and graded particles, and observed that with the increase of particle size, angle of internal friction angle increases for both uniform sands and graded sands (Islam et al. 2011).

Geosynthetics have been used for many years to provide reinforcement to many geotechnical structures such as retaining walls, slopes, embankments, pavements, railway tracks, and foundations since they provide enhanced confinement to the soil by increasing its strength and stiffness with additional advantages of improved longevity, low costs, better serviceability and earthquake resistance (Ferreira et al. 2016; Holtz 2017; Javankhoshdel and Bathurst 2017; Rowe and Ho 1998; Song et al. 2018). Geogrids are a type of geosynthetics. Many past literatures already discussed the benefits of using geogrid by considering subgrade conditions, number of geogrid layers, geogrid installation depth, presence of moisture, aggregate size to geogrid aperture size ratio, and geogrid aperture shape (Bathurst and Raymond 1987; Brown, Kwan, and Thom 2007; Chen, McDowell, and Thom 2012; Indraratna et al. 2006; McDowell et al. 2006; Mishra et al. 2014; Raymond and Ismail 2003).

One important condition that must be met when performing experiments or simulations on the effects of particle size is to make sure that the initial void ratio/porosity remains the same for the different gradations. Some research pertaining to particle size effects on shear strength parameters was not reliable because this condition was not met (Gupta 2016; Sitharam and

Nimbkar 2000). A reason for the contradictory results is that it is difficult to single out one factor from others, and on occasion, the models did not correctly reflect the working condition of the soil, especially when using a fixed boundary for triaxial DEM models.

Objectives

Based on the preceding records of inconsistencies, this thesis addresses the need for further study on the effects of particle size on the strength and strain properties of granular soil. To close this information gap, this thesis presents DEM simulations on triaxial tests with flexible membranes used to investigate the impacts of particle size on the stress-strain behaviors and strength and strain properties of soil. The developed DEM model, verified with experimental data, can create soil specimens with the same porosity, and can single out individual factors that affect soil strength and strain properties. This research is also an important first step toward modeling the stress-strain behaviors of reinforced soil in a mechanically stabilized earth (MSE) retaining wall or in a geosynthetic reinforced soil (GRS) mass.

There were limited reported study found that used flexible membrane in their DEM analyses of GRS soil. It should be noted that the objective of this study is not to discuss the reinforcing mechanisms, but rather to demonstrate a preliminary work on the capabilities of the DEM approach in modeling triaxial testing of reinforced soil specimen using a flexible membrane. Accordingly, further research is required to fully investigate both the grid and particle size, shape, and gradation effects on the overall geogrid reinforcement mechanism.

CHAPTER II

LITERATURE REVIEW

For a laboratory triaxial test, a flexible rubber or latex membrane is usually used to cover the specimen for the application of hydrostatic confining pressure. With this flexible boundary, triaxial shearing causes substantial bulging which in turn results in the formation of the shear failure bands. When simulating the laboratory test using DEM, if the rigid boundary was used, the specimen was created within that rigid boundary, which means the bulging condition could not be observed. Movement of the rigid wall was controlled by a servomechanism to maintain a constant confining pressure (σ_3), and the shear band at the end of simulation could not be observed. These issues were addressed by using a flexible membrane; however, modeling a flexible membrane is complicated and computationally expensive. Figure 1 shows a triaxial test before and after triaxial shearing with the typical bulging shape. Using flexible membrane modeling, the failure surfaces and shear bands can be viewed clearly. Qu et al. (2019) mentioned two major difficulties in modeling latex/rubber membranes during triaxial testing by DEM: (1) the precise application of hydrostatic confining pressure while simultaneously (2) ensuring the free deformation of the membrane boundary (Qu et al. 2019). This problem has led to the creation of different methods for modeling a flexible membrane in DEM by researchers wanting to better understand the behaviors of soil.

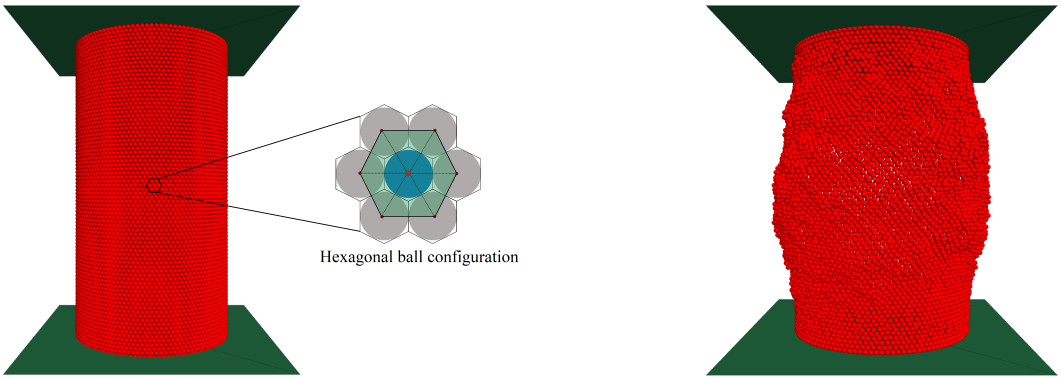

(a) Specimen before shearing (b) Specimen after shearing

Figure 1. Flexible boundary before and after shearing

Stack Wall Method

Zhao and Evans (2009) utilized several stress-controlled rigid planar walls (stack wall) to confine specimens by controlling their individual velocities by a numerical servomechanism (Zhao Xueliang and Evans T. Matthew 2009). Li et al. (2015) also used this method to simulate the torsional shear test (Li, Zhang, and Gutierrez 2015). Later, Khoubani and Evans (2018) significantly improved the flexibility of the stacked-wall boundary (Khoubani and Evans 2018), however, this approach only created a semi-flexible membrane as the walls continued to move in a horizontal direction instead of the vertical direction. Thus, the method cannot replicate the 'clamped' effects at the two ends of the triaxial specimen as discussed by Qu et al. (2019) (Qu et al. 2019).

Method of Applying Forces on Boundary Particles

Equivalent forces of confining stress are calculated and applied to the outermost particles which act as the membrane. Bardet and Proubet (1991) first introduced this technique in DEM modeling of triaxial testing (Bardet and Proubet 1991) and later other researchers proposed algorithms to improve this method (Cheung and O'Sullivan 2008; Wang Yuannian and Tonon Fulvio 2009). Cheung and O'Sullivan (2008) used the Voronoi polygon projection technique to sort out the periphery particles of the specimen to label it as a boundary to apply hydrostatic confining pressure (Cheung and O'Sullivan 2008). However, the main disadvantage of this method is that the properties of membrane and the specimen particles cannot be assigned independently, and all the particles are treated as the same material. Binesh et al., (2018) proposed a new algorithm based on linking MATLAB and PFC^{3D} codes to identify the boundary particles by using cellular division and irradiation from the specimen's centerline; then, confining pressure is exerted directly to boundary particles via concentrated forces (Binesh, Eslami-Feizabad, and Rahmani 2018). However, the proposed algorithm cannot replicate the Latex membrane in triaxial tests, since confining forces are exerted directly to the boundary particles.

Bonded-Ball Method

This method was used by Iwashita et al. (1998) to model flexible membranes to simulate biaxial simulation (Iwashita Kazuyoshi and Oda Masanobu 1998). Such a flexible membrane was composed of spherical balls that were 'glued' together with contact bonds. Bono et al. (2012 and 2014) were able to use a similar technique to model flexible membrane and thereby simulate

triaxial tests (de Bono and McDowell 2014; de Bono, Mcdowell, and Wanatowski 2012). Similar results were reported in other studies (Cil and Alshibli 2014; Lu, Li, and Wang 2018). The bonded-ball approach allows assigning specific properties to the boundary particles (i.e. different from specimen particles). The confining pressure was applied by converting the confining pressure to equivalent forces as described by Cil and Alshibli (2014) (Cil and Alshibli 2014). Membrane particles are first modeled as a cage; then, specimens are created separately inside that cage. Lu et al. (2018) were able to significantly improve the flexibility of the bonded-ball flexible membrane, which confirmed the possibility of observing a typical bulging shape of the specimen during axisymmetric triaxial compression tests (Lu et al. 2018).

Because the bonded-ball method can assign properties to boundary particles, replicating clamped effects and allowing possible specimen bulging, this method was adopted to model a flexible membrane for this research. Specifics on modeling the bonded-ball flexible membrane follow.

Geometrical Arrangement

Single layer hexagonal packing is used to obtain the closest packing to mimic the Latex membrane which has a continuous surface. Saussus and Frost (2000) noted that membrane particles should be chosen carefully to minimize the effects of the sand-membrane contact pattern (Saussus and Frost 2000). Single-layer hexagonal packing reduces the bonded-ball gaps and makes the modeled membrane as smooth as possible. Hexagonal ball packing of the flexible membrane is shown in Figure 1.

Boundary Condition

In a laboratory triaxial test, the two ends of the specimen are fixed inside a rubber vessel. When confining pressure is applied, movement of the soil particles at the two ends is restricted to

the radial horizontal direction, causing clamped effects (Qu et al. 2019). To replicate the clamped effects, the radial horizontal movement of the specimen particles at the top and bottom are restricted. For this study, the specimen material was first created within the rigid cylinder which eventually was replaced by the flexible bonded-ball membrane. The membrane is defined as the boundary of the DEM model where the confining pressure is applied.

Selection of Contact Model

A Latex membrane is "strain dominant" and cannot resist bending. Potyondy and Cundall (2004) described the bonded particle methodology, stating that a "*linear contact bond"* contact model can properly mimic the mechanism similar to that of the membrane (Potyondy and Cundall 2004). In this study, the linear contact bond is used to model the flexible membrane. This linear contact bond consists of two components: the linear component and the dashpot component, and they act parallel to each other. The linear component provides linear elastic and frictional behavior but does not resist tension, while the dashpot component provides the viscous behavior that dampens force and accounts for energy loss. Contact stiffness can be divided into two micro-parameters, normal stiffness (k_n) and shear stiffness (k_s) which act as linear springs for the linear component. For the dashpot component, the dashpot force is controlled by the normal (β_n) and shear (β_s) critical-damping ratios. Another micro parameter is the particle friction coefficient (μ) which is responsible for developing the force that resists slip between particles.

The selection of values for normal and shear stiffness for a flexible membrane has strong effects on the deformation of the membrane. Contact stiffness of membrane particles is determined based on the equivalence of strain energy and the elastic parameters of a physical Latex membrane, which was introduced by Griffiths and Mustoe (2001) (Griffiths and Mustoe

2001). Figure 2a provides a schematic diagram of the linear contact model microparameters. Because the rubber membrane must not tear apart during testing, large values of shear and tensile strength were used, which helped the membrane withstand all possible deformations.

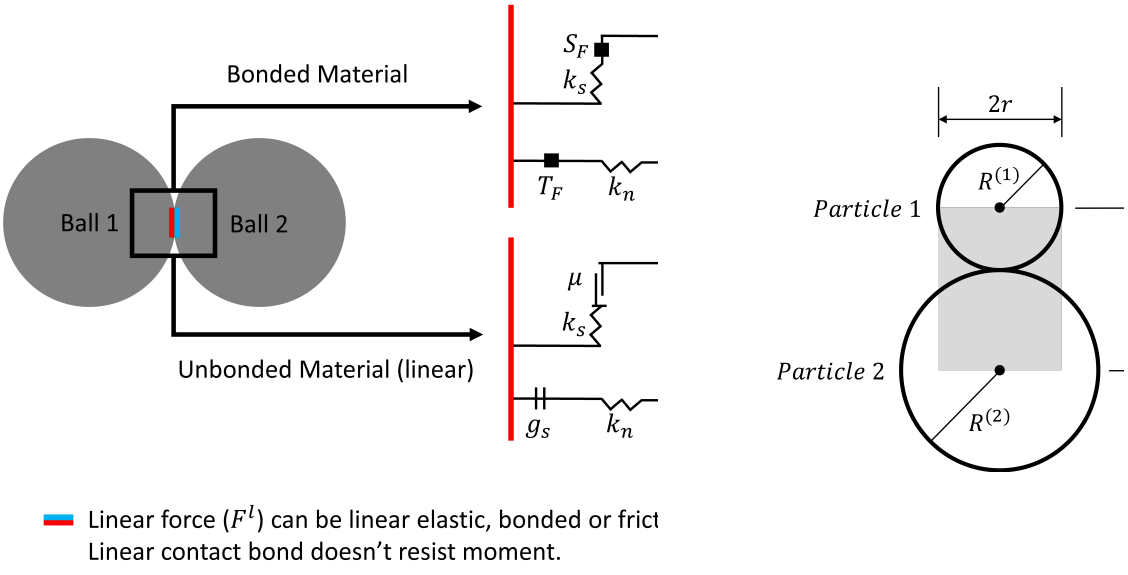

(a) (b)

Figure 2. Micromechanical model and rheology of particle contact (a) Components of the linear contact bond and (b) volume associated with contact (Itasca 2014)

Reinforcing Mechanism of Geogrid

The reinforcing mechanism generally develop by the interlocking between the geogrid and the specimen particles which depends on the properties of the geogrid and specimen particles that includes particle size and shape, geogrid types and properties (e.g. apertures, shapes and sizes of ribs), degree of compaction, and loading conditions (Qian et al. 2015). Besides, many studies have already reported the interaction mechanism between geogrid and the surrounding soil particles (Bathurst and Ezzein 2015, 2016, 2017; Cardile et al. 2017; Demir et al. 2013;

Esmaeili, Zakeri, and Babaei 2017; Ezzein and Bathurst 2014; Lin et al. 2013; Moraci and Recalcati 2006; Mousavi, Gabr, and Borden 2017; Palmeria and Milligan 1989; Saha Roy and Deb 2017; Shin and Das 2000; Sitharam and Sireesh 2004). Some researchers performed pull-out tests and direct shear tests to identify the reinforcing mechanisms of geosynthetic (Palmeira 2009; Sadat Taghavi and Mosallanezhad 2017; Wang, Jacobs, and Ziegler 2014, 2016; Zhou et al. 2012).

Laboratory Experiment

The experimental results are important for better designs of geogrid reinforced soil structures. Numerous laboratory experiment has been conducted to investigate the geogrid reinforcing effects. Researchers have been paying attention to investigate the influences of geogrid type, number of geogrid layers, vertical spacing between geogrid layers, geogrid length and depth, relative density of soil, and soil particle sizes on the responses of reinforced soil slopes loaded with strip footings (Alamshahi and Hataf 2009; Allen and Bathurst 2002; Benjamim, Bueno, and Zornberg 2007; Bergado et al. 1994; Chen and Yu 2011; Demir et al. 2013; El Sawwaf 2007; Keskin and Laman 2014; Tavakoli Mehrjardi, Ghanbari, and Mehdizadeh 2016; Xie and Yang 2009; Xue et al. 2014; Zhang et al. 2017). Jacobs and Ziegler (2016) conducted biaxial compression tests to study the effects of number of longitudinal and transverse ribs of geogrid (Jacobs and Ziegler 2016).

Xiao et al. (2016) performed a series of model tests on geosynthetic-reinforced soil (GRS) walls to investigate the effects of offset distance of a strip footing, width of the strip footing, geogrid length and connection mode between geogrid and facing on the ultimate bearing capacities of the strip footings on GRS walls (Xiao, Han, and Zhang 2016). Ahmadi and Bezuijen (2018) reported the different performance of retaining walls with rigid and flexible wall

faces under strip footing loads based on small-scale model tests (Ahmadi and Bezuijen 2018). Skejic et al. (2018) reported the influence of reinforcement strength and geometry on the failure mechanism of reinforced soil walls loaded with a strip footing (Skejic, Medic, and Dolarevic 2018). Pham (2009) performed five field-scale soil-geosynthetic composite (SGC) tests to assess the effect of reinforcement spacing and reinforcement strength on the performance of the SGC mass under plane strain condition (Pham 2009). Many experiments have also been done under above mentioned condition to quantify the performance of GRS structures such as retaining walls, and abutments (Ketchart and Wu 1996; Kongkitkul, Hirakawa, et al. 2007; Kongkitkul, Tatsuoka, and Hirakawa 2007). Xu et al. (2019) showed that the ultimate bearing capacity of the GRS mass was significantly affected by the friction angle of backfill soil, reinforcement spacing and strength (Xu, Liang, and Shen 2019).

Numerical Simulation

Numerical analysis has gained the ability to sufficiently predict the GRS soil behavior. Several studies have used Finite Element (FE) methods to analyze geogrid-reinforced structures that have been reported in the literature (Hussein and Meguid 2016; Kumar and Sahoo 2013; Li et al. 2012; Ling and Liu 2009; McDowell et al. 2006; Mosallanezhad et al. 2016; Perkins and Edens 2003; Rowe and Liu 2015; Tran, Meguid, and Chouinard 2013; Yogarajah and Yeo 1994; Zhuang and Wang 2016). However, most of these studies adopted simplifying assumptions related to either the details of the geogrid geometry or the constitutive model of the geogrid material. Besides, one inherent limitation of FEM method is the difficulty to analyze the soil-geogrid interaction at the particle level.

However, Advantages of two–dimensional (2D) and three–dimensional (3D) DEM simulations in capturing the kinematic behavior of granular material at the particulate level has

been discussed in several studies (Effeindzourou et al. 2017; Gao and Meguid 2018; Jiang, Li, and Shen 2016; Lai and Chen 2017; Shen et al. 2017; Stahl et al. 2014; Stahl and Konietzky 2011; Wang et al. 2016). Furthermore, Qian et al. (2015) simulated DEM cylindrical triaxial for soil specimens having both triangular and square shaped apertures to evaluate the improved stress-strain behavior and shear strength properties (Qian et al. 2015). The above studies demonstrated that the stress-strain behavior of a geogrid material embedded in backfill soil is complex. McDowell et al. (2006) modelled the interaction between geogrid and ballast by simulating pull-out and cyclic triaxial tests (McDowell et al. 2006). Bhandari and Han (2010) developed a DEM model to investigate the geotextile-soil interaction under a cyclic vertical load (Bhandari and Han 2010). Lin et al. (2013) analyzed the properties of sand reinforced with horizontal and vertical elements using the DEM (Lin et al. 2013). Therefore, DEM has been widely used to investigate the geogrid-soil interaction.

Additionally, Wang et al. (2016) used DEM simulation to quantify the effects of transverse ribs of geogrid on the geogrid-soil interaction (Wang et al. 2016). Miao et al. (2017) modelled DEM simulation of the pullout behavior of geogrid reinforced ballast by considering the effect of the particle shape (Miao et al. 2017). Ngo et al. (2017) studied the interface behavior of geogrid-reinforced soil through a series of discrete element simulations and reported that shear strength of the interface is governed by the geogrid characteristics, including geometry and opening size (Ngo, Indraratna, and Rujikiatkamjorn 2017). Gao and Meguid (2018) reported in their DEM simulation that the uppermost layer provides larger deformations and tensile strains compared to the lower layer in case of multi geogrid layer in triaxial specimens (Gao and Meguid 2018). Xu et al. (2020) concluded that the dilation of the backfill soil was suppressed by reinforcement and the suppression was enhanced by increasing reinforcement stiffness and

reducing reinforcement spacing in their DEM study of triaxial test (Xu et al. 2020). The above DEM investigations indicated that the DEM can be used as a practical tool to study the geogrid reinforcing effects at the particulate level.

CHAPTER III

METHODOLOGY

The PFC^{3D}, a DEM software, was utilized to study the effects of particle sizes on the soil strength and strain properties by modeling triaxial tests. Details of the approaches and methodology of the modeling follow.

Contact Stiffness of the Specimen

In this study, the specimen particles are considered as made from a linear material, and the particles are in contact but unbonded at contact. The contact force is divided into linear and dashpot components. The linear component provides linear elastic (no-tension), frictional behavior. Linear force is produced by linear springs with constant normal stiffness (k_n) and shear stiffness (k_s). The linear springs cannot sustain tension, and slip is accommodated by using the friction coefficient (μ). A more detailed description of the contact models is available in Itasca's (2014) online manual (Itasca 2014).

In the tested specimen, the normal stiffness k_n and shear stiffness k_s are set based on a specified contact deformability method. In other words, the k_n and k_s of a homogeneous, isotropic, and well-connected granular assembly experiencing small-strain deformation can be derived from the effective modulus (E^*) and the normal-to-shear stiffness ratio (k^*) at the contact (Itasca 2014),

$$k_n = \frac{AE^*}{L}; \quad k_s = \frac{k_n}{k^*} \tag{1}$$

$$A = \pi r^2 \text{ (in 3D)} \tag{2}$$

where r is the smaller value of $R^{(1)}$, and $R^{(2)}$ and L is the summation of $R^{(1)}$ and $R^{(2)}$ (Fig. 2b).

Contact Stiffness of the Flexible Membrane

Micro properties of the bonded-ball membrane are calibrated to get a stress-strain response similar to that of a smooth rubber membrane surface. One solution is to match the energy that dissipates from a unit cell of the bonded-ball membrane to the energy of the corresponding rubber membrane area (Ostoja-Starzewski 2002). The center particle of a unit cell is in contact with six neighboring unit cells (Fig. 1); thus, the total energy stored in a unit cell U_{cell} can be calculated as follows:

$$U_{cell} = \sum_c^6 U^c = \frac{L_c^2}{4} \sum_c^6 \left[K_n \varepsilon_{ij}^c l_{2j} l_{2i} \varepsilon_{kl}^c l_{2k} l_{2l} + K_s \varepsilon_{ij}^c l_{2j} (l_{1i} + l_{3i}) \varepsilon_{kl}^c l_{2l} (l_{1k} + l_{3k}) \right] \tag{3}$$

where, L_c, ε_{ij}^c, and U^c are the contact distance, equivalent strain, and equivalent strain energy for each contact c, respectively; and l_{ij} represents the cosine angle between the global and local coordinate axes. Strain energy density can be computed from the volume of the unit cell (V_{cell}). The surrounding area is represented as one-third of the equilateral triangle (Fig. 1) by joining two adjacent corners, and the area of each unit cell can be calculated as:

$$v = 2\sqrt{3} r^2 \tag{4}$$

where r is the radius of bonded membrane particle. If the thickness of the membrane equals to t, then the volume of the unit (V_{cell}) cell is:

$$V_{cell} = 2\sqrt{3} t r^2 \tag{5}$$

The distance between two particles equals two times the ball radius ($L_c = 2r$), and the strain energy density is:

$$u_{cell} = \frac{U_{cell}}{V_{cell}} = \frac{\sqrt{3}}{6t}\sum_c^6\left[K_n\varepsilon_{ij}^c l_{2j} l_{2i}\varepsilon_{kl}^c l_{2k} l_{2l} + K_s\varepsilon_{ij}^c l_{2j}(l_{1i} + l_{3i})\varepsilon_{kl}^c l_{2l}(l_{1k} + l_{3k})\right] \quad (6)$$

It is assumed that the corresponding strain tensor in a unit cell stays uniform so that the local strain is equal to the overall strain in a unit cell $\left(\varepsilon_{ij} = \varepsilon_{ij}^c\right)$. The stress tensor of a combined discrete body can be formulated by differentiating the strain energy density for the corresponding strain tensor as follows:

$$\sigma_{ij} = \frac{\partial u_{cell}}{\partial \varepsilon_{ij}} = \frac{1}{V}\frac{\partial \sum_c^6 U^c}{\partial \varepsilon_{ij}} = \frac{1}{V}\sum_c^6 \frac{\partial U^c}{\partial \varepsilon_{ij}} = \frac{1}{V}\sum_c^6 \frac{\partial U^c}{\partial \varepsilon_{ij}^c} = \frac{\sqrt{3}}{3t}\sum_c^6\left[K_n l_{2j} l_{2i}\varepsilon_{kl}^c l_{2k} l_{2l} + K_s l_{2j}(l_{1i} l_{3i})\varepsilon_{kl}^c l_{2l}(l_{1k} + l_{3k})\right] \quad (7)$$

Similarly, the elastic stiffness tensor at each contact point of bonded balls is calculated by differentiating the stress tensor for the strain tensor as follows:

$$C_{ijkl} = \frac{\partial \sigma_{ij}}{\partial \varepsilon_{kl}} = \frac{1}{V}\sum_c^6 \frac{\partial^2 U^c}{\partial \varepsilon_{ij}^c \partial \varepsilon_{kl}^c} = \frac{\sqrt{3}}{3t}\sum_c^6\left[K_n l_{2j} l_{2i} l_{2k} l_{2l} + K_s l_{2j}(l_{1i} + l_{3i}) l_{2l}(l_{1k} + l_{3k})\right] \quad (8)$$

As a result, the analytical solution for calculating the normal stiffness (K_n) and shear stiffness (K_s) of the membrane particles can be formulated as

$$K_n = \frac{Et}{\sqrt{3}(1-\upsilon)} \quad (9)$$

$$K_s = \frac{Et(1-3\upsilon)}{\sqrt{3}(1-\upsilon^2)} \quad (10)$$

where E, t, and υ are the elastic membrane modulus, the thickness of the membrane, and Poisson ratio in the whole flexible membrane system, respectively (Qu et al. 2019).

Steps for Modeling Triaxial Tests Implementing Bonded-Ball Flexible Membrane

This algorithm was developed by incorporating the membrane forming technique described by Lu et al. (2018) and Qu et al. (2019) (Lu et al. 2018; Qu et al. 2019). The steps are as follows.

1. Specimen particles are generated in a rigid cylindrical wall.
2. All the linear and rotational velocities of the specimen particles are set to zero; then, the original rigid cylindrical wall is deleted.
3. A hexagonal bonded-ball membrane is installed, and the linear contact bond is activated between membrane particles.
4. The velocity of membrane particles is fixed (i.e., no movements). Start an 'iteration' process allowing the specimen particles to move freely until a static equilibrium state is achieved.
5. An equivalent static force is converted from the confining pressure and applied to the membrane particles to maintain the constant hydrostatic pressure in the specimen.
6. Perform iterations until the whole system achieves a static equilibrium.
7. The vertical loading is applied to the specimen using a servomechanism. The servomechanism is implemented by controlling the movement of the walls using a constant velocity.
8. A rate displacement of 0.05 mm/s is applied to the top and bottom wall, which is slow enough to maintain a quasi-static condition.
9. The triaxial loading process stops when the axial strain reaches the prescribed value of 6%.

Stress-Strain Calculations for the Specimen with the Flexible Membrane

Stress is a continuum quantity and does not exist at any point in a discrete medium of particle assembly. Instead, contact forces and displacements are used to study the material behaviors on a microscale in the PFC model. The average stress in a certain region with volume V in the static condition is:

$$\overline{\sigma} = -\frac{1}{V}\sum_{N_c} F^{(c)} \times L^{(c)} \qquad (11)$$

where N_c is the total number of contacts within the volume, $F^{(c)}$ is the contact force vector, and $L^{(c)}$ is the branch vector joining the centroids of the two bodies in contact. The negative sign indicates the compressive stress to the system.

A bonded-ball flexible membrane has an uneven surface, which makes it more difficult to calculate the volume of the deformed specimen compared to that of a rigid membrane. The logarithmic value of strain is useful to quantify the distortion due to loading in this case. The axial strain, $\varepsilon_1$can be calculated as:

$$\varepsilon_1 = -\int \delta\varepsilon = -\int_{H_0}^{H} \frac{\delta H}{H} = -\ln\left(\frac{H}{H_0}\right) = \ln\left(\frac{H_0}{H}\right) \qquad (12)$$

and, the volumetric strain, ε_V can be calculated as:

$$\varepsilon_V = -\int \delta\varepsilon_V = -\int_{V_0}^{V} \frac{\delta V}{V} = -\ln\left(\frac{V}{V_0}\right) = \ln\left(\frac{V_0}{V}\right) \qquad (13)$$

where H and V are the current height and volume of the specimen, and H_0 and V_0 are the original height and volume of the specimen before starting the test. Here, compression is positive.

Geogrid Modeling

The geogrid is modeled as strings of overlapping spherical balls joined by biaxial parallel bonds (Figure 3). Parallel bonds provide the structural properties of the grid, and the spherical balls provide the surface for grid-soil interaction.

(a) (b)

Figure 3. (a) geogrid consists of strings of overlapping bonded spherical balls, (b) parallel bonds (red)

Geogrids are oriented perpendicular to the specimen axis. Grid-set properties are chosen to match with the geogrid geometry. The grid tensile stiffness is measured by the multiple aperture tensile (MAT) test. Parallel-bonded grid consists of join balls to provide junction stiffness and two intersecting ribs to meet the biaxial condition. The specimen particle-particle contacts employ the linear material (unbonded), the grid-grid contacts employ the linear parallel bond contact model, and bonded-ball flexible membrane employ the linear contact bond contact model as discussed by Pham et al. (2020) (Pham, Zaman, and Vu 2020).

Elements of the grid

Each grid rib behaves as an elastic beam of circular cross section with varying radius along its length. The grid behaves as an elastic body; it will not break, and it will return to its original shape when unloaded. The grid methodology of Stahl and te Kamp (2013) employed a parallel-bond radius and stiffness decreasing law to allow the grid to exhibit nonlinear and plastic behavior, however, the stiffness decreasing law is excluded from this study believing that grid

experiences small deformation loading for which rib tensile strains remain less than three percent and junction rotations remain less than two degrees (Stahl and te Kamp 2013).

The grid set is aligned with the specimen axis and positioned within a cylindrical flexible cell. Grid deformation causes strain energy to be stored in the contacts that join the grid balls to one another (Itasca 2014).

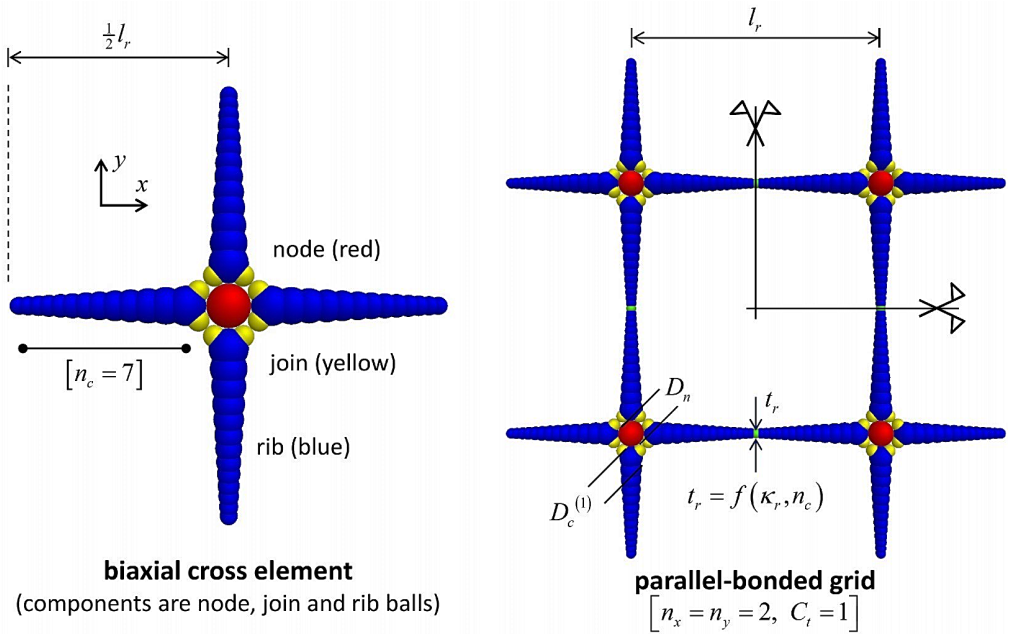

Figure 4. Cross element and biaxial parallel-bonded grid consisting of four cross elements (Itasca, 2018)

Each grid is flat and lies in the xy-plane. A grid consists of identical cross elements, with n_x and n_y cross elements in the x- and y-directions, respectively. A biaxial cross element consists of one node ball with a half rib in both directions (Figure 4).

Parallel-Bonded Grid

The geometry of a cross element is defined by the node-ball diameter (D_n), the diameter ratio of the first rib ball ($k_r = D_c^{(1)}/D_n$), the rib length (l_r), and the number of core balls per half

rib (n_c). The minimum rib thickness (t_r) is a function of k_r and n_c. The parallel-bond radii in the grid are defined by the parallel-bond radii at the node and mid rib ($\overline{R_n}$ and $\overline{R_m}$ along with an exponential variation along each half rib) and the parallel-bond radius multiplier of the join balls ($\overline{\lambda_J}$). The material properties of the grid are defined by the local-damping factor, density, effective modulus and stiffness ratio ($\alpha_g, \rho_g, E_g^*, k_g^*$). The material properties of the grid surface are defined by the grid-surface effective modulus, stiffness ratio and friction coefficient ($E_{gs}^*, k_{gs}^*, \mu_{gs}$).

The parallel bonds in the grid are assigned infinite strengths to preclude bond breakage, the parallel bond stiffnesses are set based on E_g^* and k_g^*, the parallel-bond radii at each join ball are set based on $\overline{\lambda_J}$ and join-ball diameter, and the parallel-bond radii along each half rib are set according to Eq. (22).

The balls of a cross element half rib are shown in Figure 5. The half rib consists of one node ball, two join balls, and a string of rib balls, with the rib balls being divided into core-rib balls, mid-rib balls and a tip-rib ball. The sizes of the core-rib balls satisfy the relation:

$$\frac{1}{2} l_r = \frac{1}{2} D_n + \sum_{b=1}^{n_c} \alpha^{(b-1)} k_r D_n \qquad (14)$$

This relation is rewritten in the form:

$$f(\alpha) = \frac{D_n - l_r}{2 k_r D_n} + \sum_{b=1}^{n_c} \alpha^{(b-1)} = 0 \qquad (15)$$

The constant, α, is found by solving the above expression via Newton-Raphson iteration. The diameters and positions of the rib balls are expressed in terms of alpha as follows. The diameters and positions of the core-rib balls:

$$D_c^{(b)} = \alpha^{(b-1)} k_r D_n, b \in \{1,2, \dots \dots \dots, n_c\} \qquad (16)$$

$$S_c^{(b)} = S_c^{(b-1)} + \frac{1}{2} D_c^{(b-1)} + \frac{1}{2} D_c^{(b)}, D_c^{(0)} = D_n, S_c^{(0)} = 0, b \in \{1,2, \dots \dots \dots, n_c\} \qquad (17)$$

The diameters and positions of the mid-rib balls:

$$D_m^{(b)} = \frac{2\alpha}{(1+\alpha)^2}\left(D_c^{(b)} + D_c^{(b+1)}\right), D_m^{(n_c)} = 2D_c^{(n_c)} - D_m^{(n_c-1)}, b \in \{1,2,\ldots\ldots\ldots, n_c - 1\} \quad (18)$$

$$S_m^{(b)} = S_c^{(b)} + \frac{1}{2}D_c^{(b)}, b \in \{1,2,\ldots\ldots\ldots, n_c\} \quad (19)$$

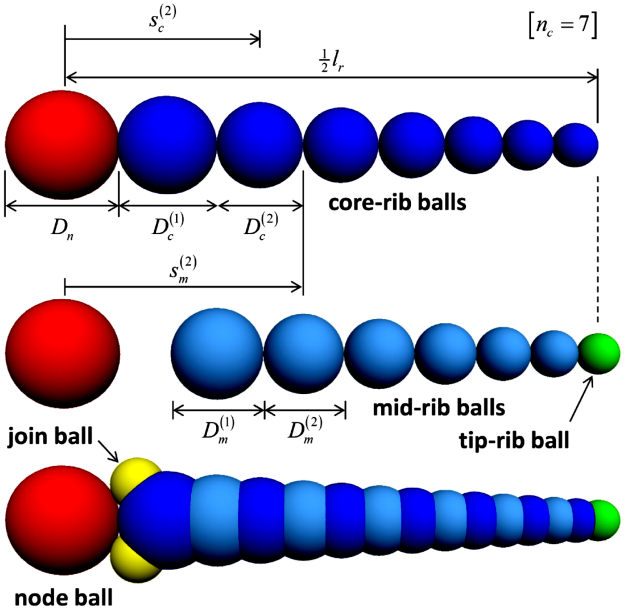

Figure 5. Cross element half rib showing node ball, join balls and rib balls (Itasca, 2018)

There is also a tip-rib ball that lies between adjoining cross elements, and its diameter and position are obtained by treating it as a mid-rib ball. The diameters and positions of the join balls are shown in Figure 6.

$$D_j = \frac{1}{2}D_n \quad (20)$$

$$\beta = \frac{\pi}{4} - \varphi, \varphi = \sin^{-1}\left(\frac{D_j}{D_n + D_j}\right) \quad (21)$$

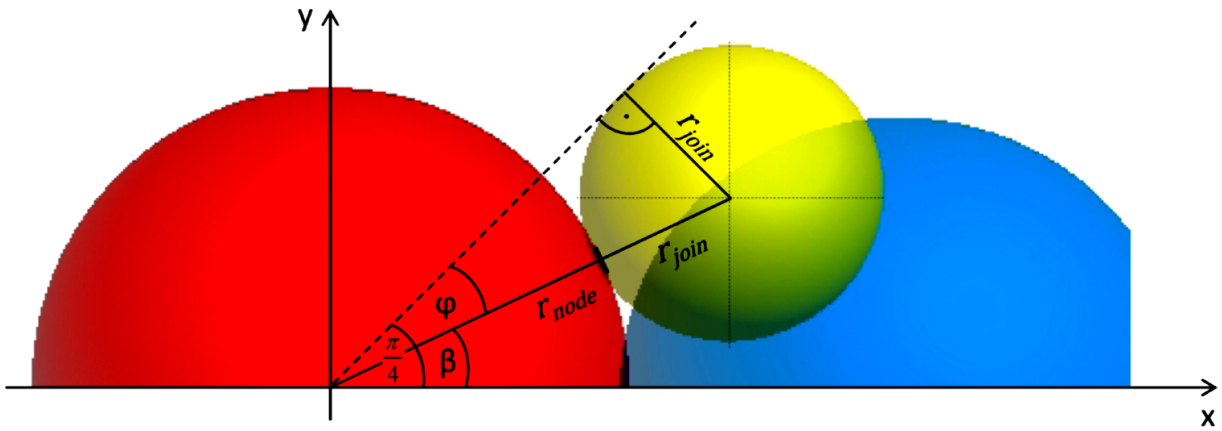

Figure 6. Cross element half rib showing location of the top join ball (Itasca, 2018)

The parallel-bond radii in the geogrid vary exponentially along each half rib (Figure 7):

$$\bar{R} = \alpha e^{bs}, \frac{1}{2}D_n \leq s \leq \frac{1}{2}l_r \qquad (22)$$

With

$$\alpha = \overline{R_n} exp\left(\frac{-bD_n}{2}\right) \qquad (23)$$

$$b = ln\left(\frac{\overline{R_n}}{\overline{R_m}}\right)\frac{2}{D_n - l_r} \qquad (24)$$

where s is measured from the node-ball center. Each join ball has four parallel bonds joining it to the node ball, the adjacent join ball, and the first two rib balls.

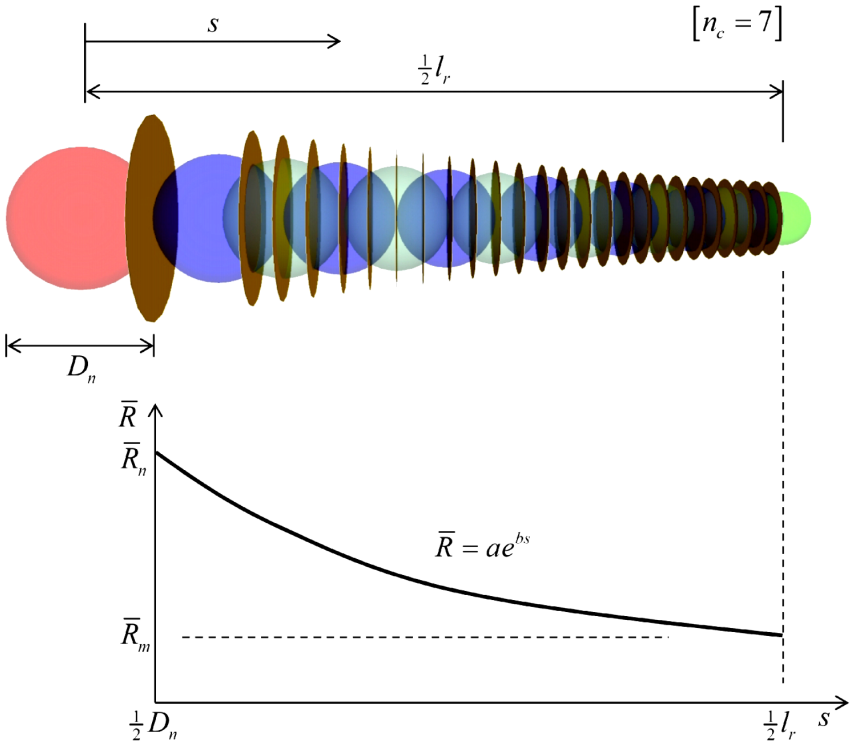

Figure 7. Cross-element half rib showing variation of parallel-bond radius from node ball to mid rib. Each parallel-bonded interface is drawn as a disk with radius equal to parallel-bond radius (Itasca, 2018)

Grid Calibration: Multiple Aperture Tensile Tests

Hussein and Meguid (2016) performed planer sheet analysis to calibrate the geogrid model (Hussein and Meguid 2016). Cheng et al. (2017) calibrated DEM model by simulating triaxial tests (Cheng et al. 2017). Gao and Meguid (2018) calibrated the governing microparameters (effective modulus, stiffness ratio, peak and residual friction coefficients) using a series of triaxial-compression and direct shear tests (Gao and Meguid 2018). Additionally, they simulated simplified flexural bending tests to determine the flexural rigidity of the geogrid material. Xu et al. (2020) calibrated their DEM model by the results of geosynthetic tensile test, angle of repose test, biaxial test, and the vertical applied pressure – settlements curves of the

GRS masses (Xu et al. 2020). Chen et al. (2020) calibrated DEM model by simulating three direct shear tests (Chen, Zhou, and dos Santos 2020).

In this study, the tensile stiffness of the geogrid is measured by performing a Multiple Aperture Tensile (MAT) test. A grid section consisting of six by six apertures is clamped along its left and right edges as shown in Figure 8. The grid is subjected to a one-percent extension. The right edge is fixed, and a constant velocity is applied to the left edge while monitoring the applied displacement (Δ) and associated force (F). The tensile stiffness is given by

$$k = \frac{F}{\Delta} \tag{25}$$

The tensile stiffness is not constant but varies as the number of apertures changes. An alternative stiffness measure that is independent of the number of apertures is the effective modulus given by

$$E' = \frac{kL}{A'} = \frac{kL}{D_n W} \tag{26}$$

where L is the horizontal distance between the clamps, A' is the effective area of the grid cross section, D_n is the diameter of the spherical node at each grid junction, and W is the effective width of the cross section. The displacement field is shown in Figure 9. The grid effective modulus is 85.4 MPa (Figure 10).

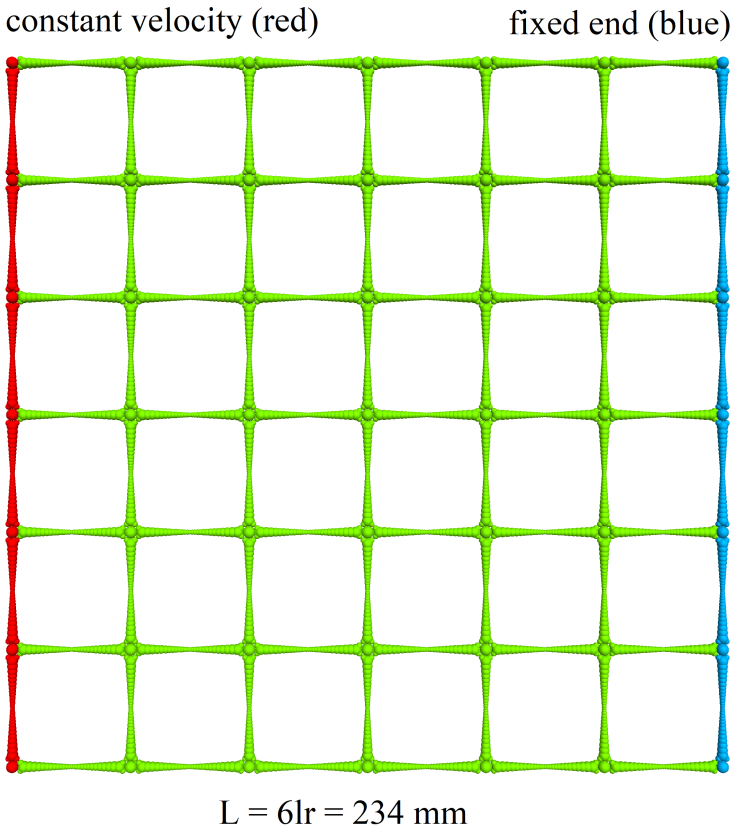

Figure 8. The SS20 parallel-bonded grid showing the boundary conditions for the MAT test.

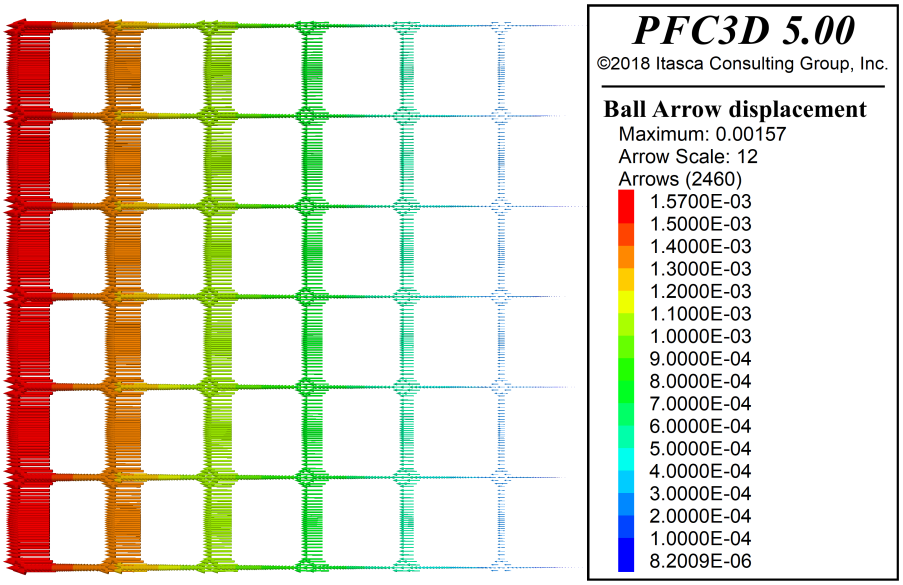

Figure 9. The displacement field of the SS20 parallel-bonded grid at the end of the MAT test after application of one-percent extension

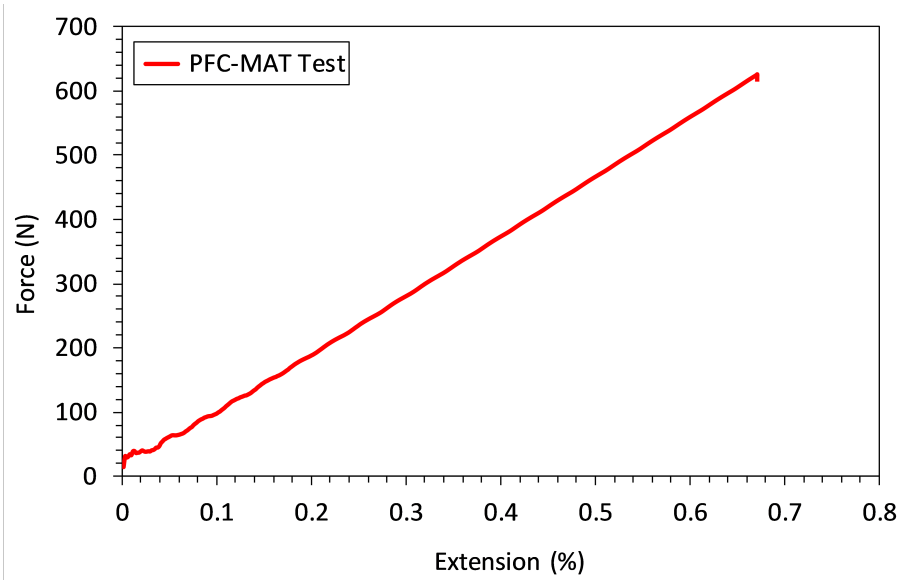

Figure 10. Strength of SS20 parallel-bonded grid at the end of MAT test

Grid-Embedment Procedure into The Flexible Membrane Model

First, grid set are created in its initial, undeformed configuration within the rigid cylindrical wall, and constrained by fixing the grid balls so that they cannot translate or rotate. The grid remains constrained until the specimen particles are generated, and hexagonal bonded-ball flexible membrane is installed replacing the rigid wall, during which the grid does not move or deform while the particles can flow around the grid. Several iterations are performed until the whole system achieves a static equilibrium. Next, the grid constraint is removed by freeing the grid balls so that they can translate and rotate in response to the compressive forces imposed by the specimen particles. Lastly, the triaxial loading process is applied until the axial strain reaches the prescribed value of 6%.

Geogrid Model Validation

The model calibration technique and precision testing of repeated runs were already discussed in the study conducted by Pham et al. (2020) (Pham et al. 2020). Geogrid is added to

the developed model to test the reinforced soil specimen in the triaxial condition. This study adopted the experimental triaxial test results for reinforced soil performed by Abu-Hassan (2006) to validate the performance of the developed model with geogrid (Abu-Hassan 2006). It should be noted that Abu-Hassan (2006) performed several experiments by varying number of geogrid layers. In this study, experimental results that involve two geogrid layers spaced at 76 mm has been taken for the DEM model validation.

For the model validation, two simulation tests were run at different confining pressures of 103, 207 KPa. Inputs of microscopic parameters used in the model include effective modulus (E^*) of 4×10^7 N/m, stiffness ratio (k^*) of 1.0, and friction coefficient (μ) of 2.0. Obtained stress-strain curves of the two simulated tests are presented along with the experimental test data from Abu-Hassan et al. (2006) in Figure 11. The curves are almost identical showing the same behaviors of the simulated specimens as of the experimental specimens. This agreement verified the PFC DEM model for the analysis. The developed model can be used to predict the nonlinear stress-strain behavior of reinforced granular materials.

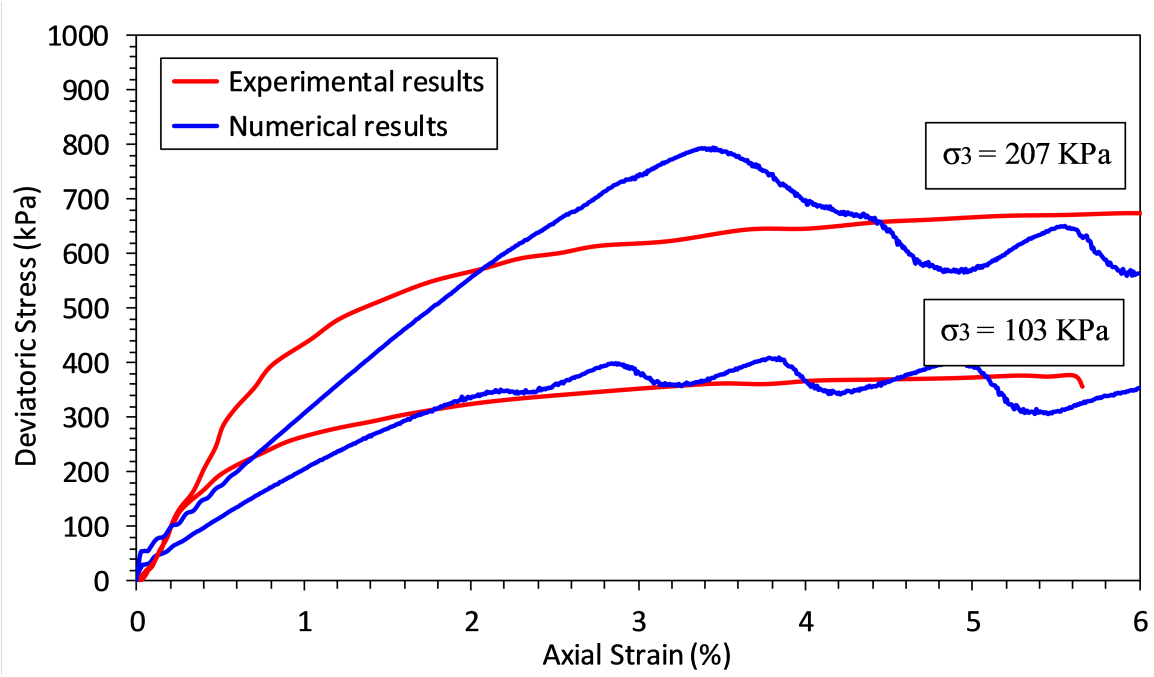

Figure 11. Comparison of experimental and numerical triaxial test results

CHAPTER IV

MODEL DEVELOPMENT CRITERIA

In a DEM triaxial test simulation, distinct differences exist between the membrane particles and the specimen particles, including size, stiffness, and geometric arrangement. To obtain more accurate results on the stress-strain responses of the specimens with a bonded-ball flexible membrane, the following criteria were maintained:

Specimen Particle Size and Membrane Particle Size

Qu et al. (2019) performed sets of uniaxial tension tests and compared them with the analytical solution to observe the modeling efficiency (Qu et al. 2019). They concluded that the numerical model with a flexible bonded-ball membrane can have less than 5% error if the following empirical rule of radius ratio is used:

$$35 \leq \frac{\mathrm{R}}{\mathrm{r}} \leq 100 \qquad (27)$$

where R is the test cylinder radius and r is the membrane ball radius. When the radius ratio is less than 35, larger gaps exist between membrane particles, and the results become unsatisfactory. On the other hand, when the radius ratio is more than 100, the number of elements is significantly large, which leads to exceptionally high computational costs.

As in a typical laboratory triaxial test, the diameter of the specimen (or the inner diameter of test cylinder D) should be at least six times greater than the maximum particle sizes d_{max}.

Membrane particles should be small enough to achieve the closest packing, which can be achieved by using smaller sized membrane particles, but the trade-off is the higher computationatime. To get satisfactory results at a reasonable computation time, Bono et al. (2012) suggested that membrane particle size may be taken as one-third of the specimen particles (de Bono et al. 2012). This ratio is used in this study.

Particle Friction Coefficient

The local friction coefficient of sand has a strong effect on the deformation of particles (Belheine et al. 2009), and the contact stiffness and friction coefficient have strong effects on shear testing results (Coetzee and Els 2009; Lommen, Schott, and Lodewijks 2014). For the calibration of sand microparameters using DEM simulations, to match the critical-state shear stress, Ahlinhan et al. (2018) used a particle friction coefficient value greater than 1.0 (Ahlinhan et al. 2018). A high value on the particle friction coefficient can compensate for the low rotational and shearing resistance of spherical particles. The high value can also account for the irregularity effects on the particle shape—to possibly increase the overall shearing resistance between spherical particles. For this study, a lower friction coefficient of 0.3 was chosen as a starting point for the model calibration, and later, to increase the interlocking between spherical particles, a higher friction coefficient larger than 1.0 was used to study the stress-strain relationship.

Application of Confining Pressure

As like a laboratory triaxial test, the hydrostatic confining pressure is applied to the membrane as isotropic stress in simulating of the test. For the bonded-ball flexible membrane

approach, the confining pressure needs to be converted to the equivalent static force that acts uniformly from all directions. Since the membrane is packed by hexagonal ball configuration, the whole system consists of a set of triangular bodies (Fig. 1). Hence, the resultant force acting on each particle can be computed from six neighboring particle triangles:

$$F^* = \frac{\sigma_{static}}{3} \sum_i^6 n_i S_i \quad (28)$$

where σ_{static} is the confining stress; n_i and S_i are the normal direction and area of the i^{th} triangle, respectively (Qu et al. 2019).

CHAPTER V

ANALYSES, RESULTS AND DISCUSSIONS

For a DEM model, there exists micro-structural input parameters that cannot be measured directly in the laboratory; thus, a common approach is to calibrate or back-calculate these micro parameters by simulating laboratory tests and adjusting these parameters to match with the experimental data. Note that the stress-strain responses of the numerical experiment are sensitive to two or more micro parameters (Coetzee 2016, 2017; Marigo and Stitt 2015), and there is no unique solution since more than one combination of the parameters may result in a similar stress-strain response. Adjusting the micro parameters was necessary for model calibration and was achieved by matching the simulation results with the experimental data. Sensitivity analyses were carried out to identify the effects of the micro-parameters on the stress-strain responses of granular soils, and based on the results, micro-parameters were selected for use in the DEM model. The model was verified using experimental data, and the analysis were carried out for the stress-strain response of the simulated triaxial tests.

Sensitivity Analysis

Sensitivity analyses were performed to identify the effects of micro-parameters on the stress-strain responses of granular soils. Two sets of numerical simulations were performed. Set 1 includes cases [1.1] to [1.5] with varying particle stiffness. Set 2 includes cases [2.1] to [2.5] with varying particle friction coefficients. Inputs for the sensitivity analysis are presented in

Table 1. The base values of the particle stiffness and friction coefficient were set to $10^6 N/m$ and 0.3 respectively. Confining pressure, σ_3, was at 100 kPa.

For Set 1, an increase was observed in particle normal stiffness and shear stiffness resulting in an increase in the material elastic modulus, shown as the slopes of the stress-strain curve increases (Figure 12a). However, changes in the normal and shear stiffness does not affect the peak strength of the curves, since there is no clear trend for the peak values in the different cases. For Set 2, it was observed that increasing the friction coefficient causes an increase in peak strength (Figure 12b). However, the increasing friction coefficient does not affect the material elastic modulus, since the slope of the curves is the same. Furthermore, an increase in friction coefficient does not affect the residual stresses of the curves either. An application of this finding is that, for the model calibration, if the desired elastic modulus is reached, then the particle friction coefficient is adjusted to match the peak strength of the numerical results with the experimental result.

Table 1. Inputs for Sensitivity Analysis

Numerical Simulations	$k_n\ (N/m)$	$k_s\ (N/m)$	$\mu\ (-)$
Base value	10^6	10^6	0.3
Case [1.1]	$k_{n1.1} = 0.1k_n$	$k_{s1.1} = 0.1k_s$	$\mu_{1.1} = \mu$
Case [1.2]	$k_{n1.2} = 0.25k_n$	$k_{s1.2} = 0.25k_s$	$\mu_{1.2} = \mu$
Case [1.3]	$k_{n1.3} = 0.5k_n$	$k_{s1.3} = 0.5k_s$	$\mu_{1.3} = \mu$
Case [1.4]	$k_{n1.4} = 0.75k_n$	$k_{s1.4} = 0.75k_s$	$\mu_{1.4} = \mu$
Case [1.5]	$k_{n1.5} = k_n$	$k_{s1.5} = k_s$	$\mu_{1.5} = \mu$
Case [2.1]	$k_{n2.1} = k_n$	$k_{s2.1} = k_s$	$\mu_{2.1} = \mu$
Case [2.2]	$k_{n2.2} = k_n$	$k_{s2.2} = k_s$	$\mu_{2.2} = 1.33\mu$
Case [2.3]	$k_{n2.3} = k_n$	$k_{s2.3} = k_s$	$\mu_{2.3} = 2.33\mu$
Case [2.4]	$k_{n2.4} = k_n$	$k_{s2.4} = k_s$	$\mu_{2.4} = 3.33\mu$
Case [2.5]	$k_{n2.5} = k_n$	$k_{s2.5} = k_s$	$\mu_{2.5} = 5\mu$

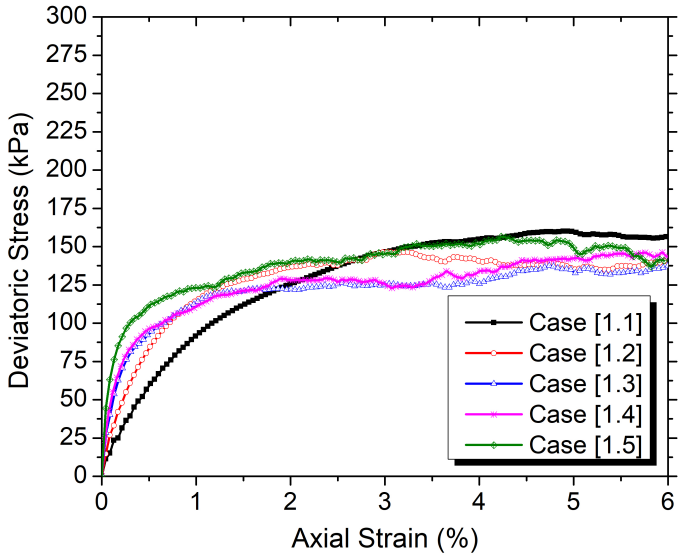

(a) Stress-strain curves for Set 1 with different particle stiffnesses, showing that the elastic modulus increases with the increasing the particle stiffness

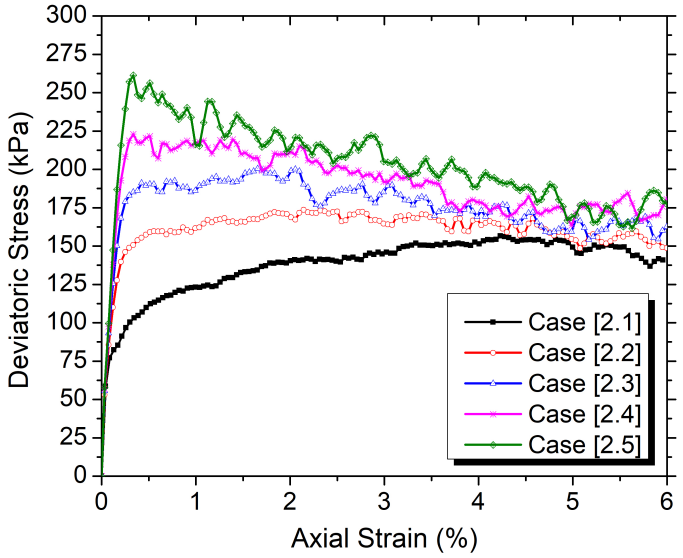

(b) stress-strain curves for Set 2 with different particle friction coefficients show how peak strength increases with increasing the particle friction coefficient

Figure 12. Stress-strain curves from sensitivity analyses

Calibrating and Validating the Model

This study adopted experimental triaxial test data of steel balls performed by Lin et al. (2016) to calibrate and validate the 3D numerical model (Lin and Zhang 2016). Numerical stiffness parameters such as normal stiffness k_n and shear stiffness k_s were determined to match the elasticity modulus (stress-strain curve for strain less than 1%) of the steel material. After achieving the target elasticity modulus, the particle-particle friction coefficient (μ) was varied to adjust the peak stress of the numerical results.

For the model validation, three simulation tests were run at different confining pressures of 100, 300, and 500 KPa. Inputs of microscopic parameters used in the model include normal stiffness of 7×10^5 N/m, shear stiffness of 3×10^5 N/m, and friction coefficient of 0.3. Obtained stress-strain curves of the three simulated tests are presented along with the experimental test data from Lin et al. (2016) (Lin and Zhang 2016) in Figure 13a. The curves are almost identical showing the same behaviors of the simulated specimens as of the experimental specimens. The model's precision was tested by running three samples two time each. These tests showed the stress-strain curves of the repeated runs to be identical (Fig. 13b). This agreement verified the PFC DEM model for the analysis. The developed model can be used to predict the nonlinear stress-strain behavior of granular materials.

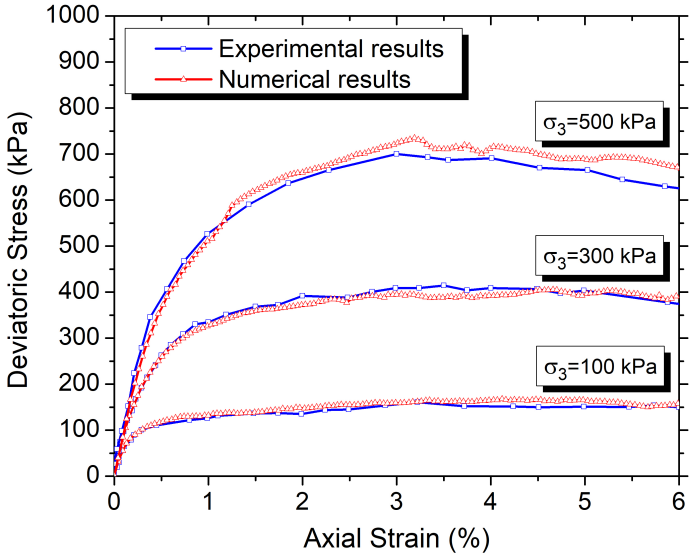

(a) Comparison of experimental and numerical data showing the model's accuracy

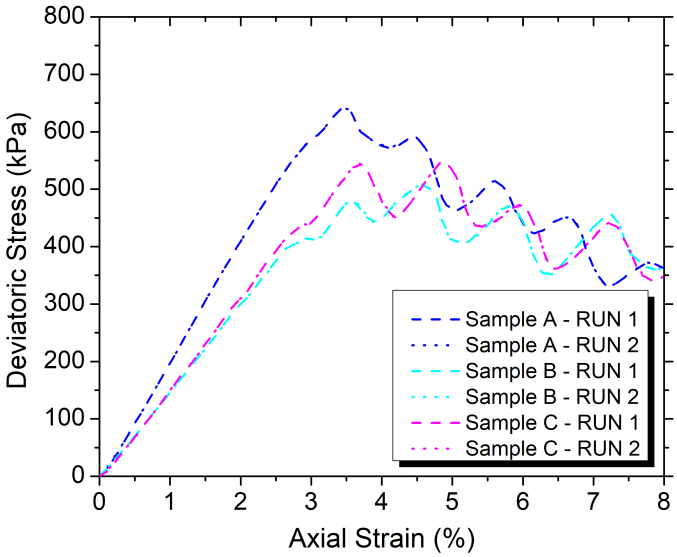

(b) Repeated runs with identical results showing the model's precision.

Figure 13. Validation and precision of the DEM model

Effects of particles size on deviatoric stress, friction angle, and dilatancy angle

The model shows its potential to isolate individual factors that affect soil strength and strain properties. These factors may include particle size, shape, and surface smoothness. For this study, the effects of particle size on stress-strain behaviors, deviatoric stress, friction angle, and dilatancy angle were investigated. Four scenarios were considered covering soil with randomly created particle sizes, soil with uniform particle size, and two soils, each with two different particle sizes, as follows:

- Case I: Soil with randomly created particle sizes. In this case, the minimum particle size was not changed while the maximum particle size was increased. In between are randomly created particle sizes. The focus here was a study on the effects of the presence of larger particle sizes and the mean particle size D_{50} on the three parameters of deviatoric stress, friction angle, and dilatancy.
- Case II: Soil with uniform spherical particles. The particle size was increased from 4 mm to 12 mm to study the effects of particle size on the three parameters.
- Cases III and IV: The focus here was on soil consisting of only two particle sizes, the smaller diameter, D_S, and larger diameter, D_L. Smaller particles with diameter D_S make up 90% of the specimen volume. Larger particles with diameter D_L make up 10% of the volume. Starting with uniform soil ($D_S = D_L$) the parameters for both cases follow:
  - → for Case III: D_S was kept unchanged, and the larger diameter D_L was increased from 4 mm to 12 mm.
  - → for Case IV: D_L was kept unchanged, and smaller diameter D_S was decreased from 12 mm to 4 mm.

Soil specimens were contained in cylinders made up of bonded balls to simulate flexible membranes. The cylinders were 140 mm high and 70 mm in diameter. Microscopic parameters used in the model are shown in Table 2. The axial strain rate was 0.05 mm/s, small enough to consider the soil specimen as being in a quasi-static condition. The load is quasi-static and is applied slowly to maintain a low strain rate, allowing the system to deform slowly so that the inertia force developed in the system is negligible. The benefit of maintaining a quasi-static condition is to keep the internal pressure developed from the external compression constant and uniform.

Table 2. Microscopic Parameters

Properties	Test specimen	Membrane
Contact model	Linear	Linear contact bond
Minimum ball radius (mm)	3.0	1.0
Maximum ball radius (mm)	6.0	1.0
Density (kg/m^3)	2650	2000
Friction coefficient	4.0	0
Effective modulus (Pa)	3×10^7	1.25×10^6
Poisson ratio	-	0.2
Normal bond strength (Pa)	-	10^{100}
Shear bond strength (Pa)	-	10^{100}
k_n/k_s	1.0	k_n and k_s were calculated based on the Poisson ratio, membrane thickness, and membrane modulus

Analysis for Case I

Effects of larger particle size and D_{50} on deviatoric stress, friction angle, and dilatancy were studied by simulating triaxial tests for three soils with three specimens T1, T2, and T3. The minimum diameter was kept at 6 mm, and the maximum diameter was increased to 8 mm, 10 mm, and 12 mm (Table 3). Spherical particles with different diameters in between were randomly created to increase D_{50}. All specimens have the same porosity. The grain size distributions for the specimens are shown in Figure 14.

Table 3. Numerical Specimen Characteristics

Specimen Code	Minimum diameter, D_{min} (mm)	Maximum diameter, D_{max} (mm)	D_{50} (mm)
T1	6	8	6.87
T2	6	10	7.81
T3	6	12	9.13

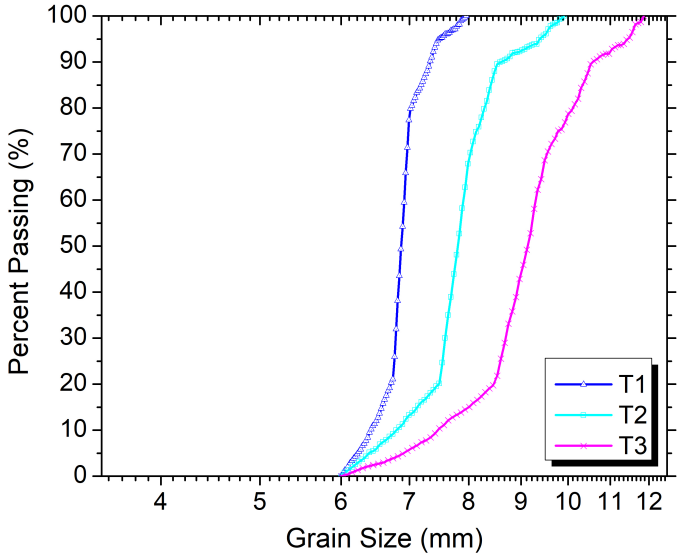

Figure 14. Grain size distribution curves for soil specimens

Figure 15a.i shows stress-strain responses of the three specimens at a low confining pressure of 35 kPa. Specimen T1's peak stress is the lowest at 130 kPa. The highest peak stress value was at 142 kPa for Specimen T3 which has the largest maximum size and highest D_{50}. An approximately 8% increase in the peak deviatoric stress was observed by varying particle sizes, showing the dependency of the shear strength on the particle diameter.

To obtain the soil strength parameter of the friction angle for the soils, additional tests with higher confining pressures of 70 kPa and 150 kPa were simulated. Similar responses were observed confirming that for this Case I, specimens with larger maximum size and D_{50} generate higher strengths (Fig. 15b.i and 6c.i). In the post-peak zone of the stress-strain curves, the specimens exhibited strain-softening behavior for all three confining pressures.

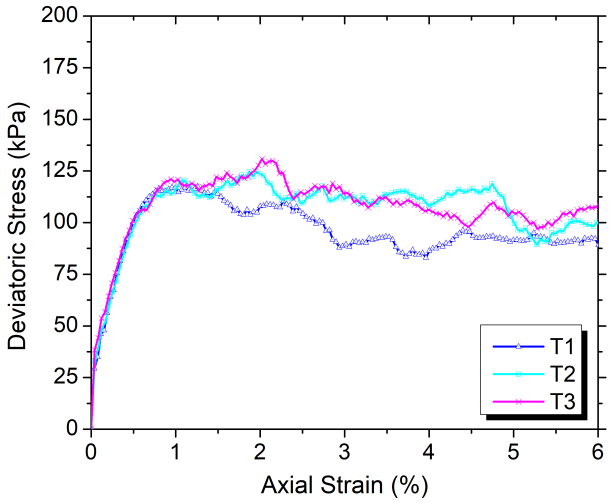

(i) Stress-strain curves.

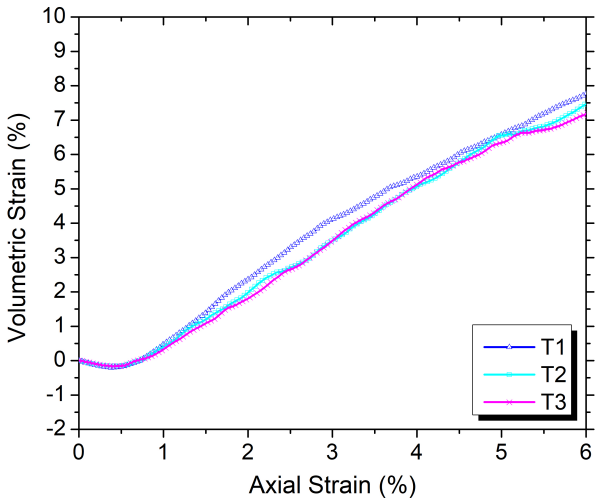

(ii) Volumetric strain.

(a) Confining pressure $\sigma_3 = 35\ kPa$.

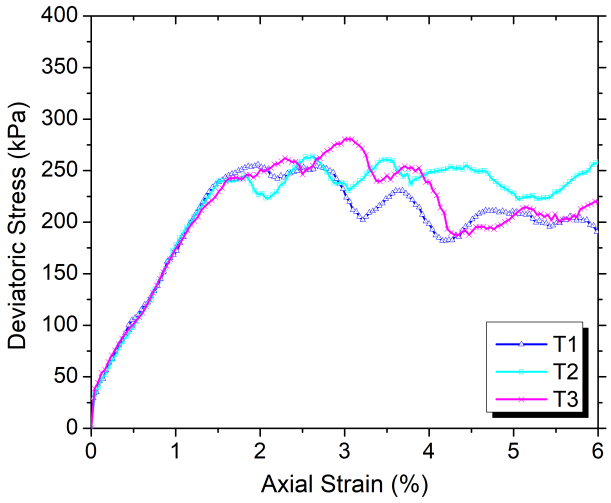

(i) Stress-strain curves.

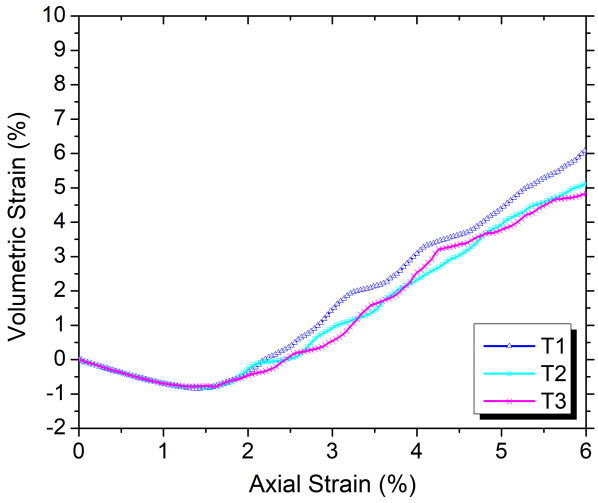

(ii) Volumetric strain.

(b) Confining pressure $\sigma_3 = 70\ kPa$.

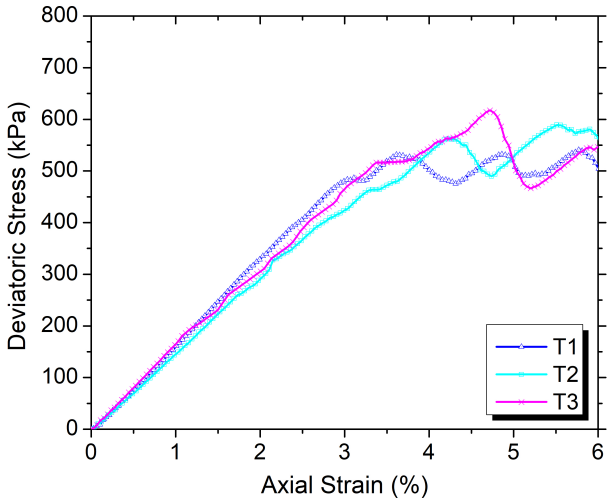

(i) Stress-strain curves.

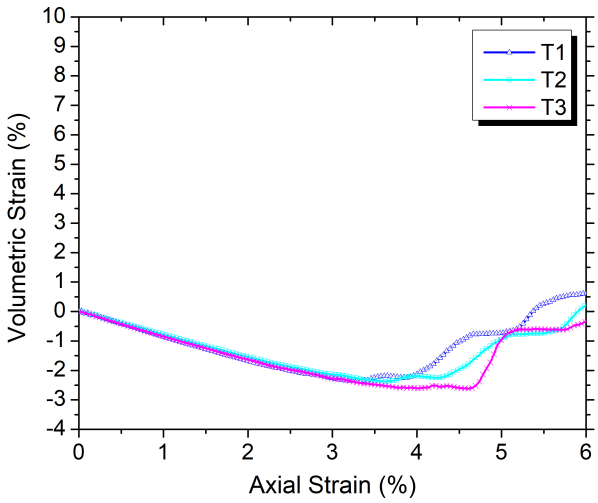

(ii) Volumetric strain.

(c) Confining pressure $\sigma_3 = 150\ kPa$.

Figure 15. Case I: stress-strain relation and volume change

Fig. 16 presents Mohr's-circles and failure envelopes for the three soil specimens. The angle of internal friction (φ) determined from the envelopes is 38.1° for T1 and increases to 42.3° for specimen T3 (Table 4). For these soils with the same minimum particle size, the larger the maximum particle size is, the higher the internal friction angle is. This is consistent with the research results reported by Dai et al. (2016) and Harehdasht et al. (2017) (Amirpour Harehdasht et al. 2017; Dai, Yang, and Zhou 2016). The finding that shear strength increases with the increase of coarse content in the specimen is in consistent with finding from Xiaofeng et al. (2013), and Kim and Ha (2014) (Kim and Ha 2014; Xiaofeng et al. 2013).

Note that each envelope is tangent with the three circles, meaning that, as in theory for cohesionless soil only one test is needed to determine the soil's failure envelope and friction angle instead of requiring several tests for a soil as in the laboratory. For the rest of the analysis, only one test at one confining pressure is analyzed to obtain the friction angle for a soil specimen.

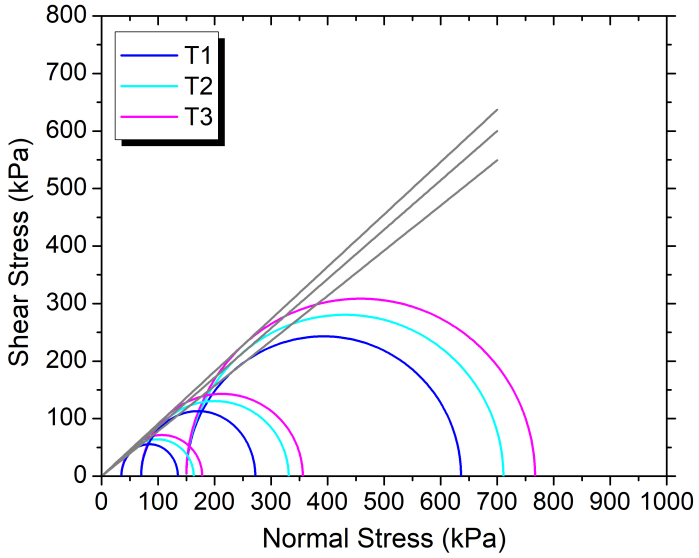

Figure 16. Mohr's Circles generated for T1, T2, and T3 with the Mohr-Coulomb failure envelopes to obtain the friction angles

Table 4. Angle of Internal Friction and Dilatancy Angle.

Specimen Code	φ (°)	Ψ (°)
T1	38.1	9.7
T2	40.6	12.9
T3	42.3	15.1

Volume change was observed for all specimens (Fig. 15). At the initial stage of triaxial shearing, all the tests share the same rate of volume contraction. This trend is due to the elastic deformation which dominates initial shearing. However, in the post-peak zone, a noticeable difference in dilation occurs. The changes in dilatancy angles for the three specimens were determined from 9.7° to 15.1° (Table 4). Dilatancy angles are increased by 35% when particle sizes are increased in these randomly created specimens, showing the presence of larger particle

sizes has strong impacts on the dilatancy of granular soil. Additional observation is the effects of confining pressures, higher confining pressure results in higher deviatoric stress, and failure occurs at larger axial strains. Also, higher confining pressure causes dilation to occur at a larger axial strain. Expansion/dilation starts to occur at around 0.6% axial strain when confining pressure is at 35 KPa and may reach up to 4% with the confining pressure of 150 KPa.

The observation that those specimens, with the same minimum particle size and same porosity but have the presence of larger particles, being capable of producing a higher resistance to shear can be qualitatively explained. During shear testing, the external load is transferred in a granular specimen by forming local contact forces at contact points. Particles in the granular specimen gradually move to a new arrangement during shearing. The relative movement of larger particles is less than that of the smaller particles since the smaller particles have the tendency to fill in the voids. The movements lead to continuous breaks and a reconstruction of contacts. Since the load is strain-controlled, and the larger particles move less, the stress concentrates more and more on the larger particles' contacts, resulting in more load is carried by the larger particles. For this Case I soil with gradation, the deviatoric stress, friction angle and dilatancy angle all increased as the mean particle size D_{50} increased.

Analysis for Cases II, III and IV

Soil for Case II has uniform spherical particles. Soil for Cases III and IV has two particle sizes, smaller particles with diameter D_S, which makes up 90% of the specimen volume, and larger particles with diameter D_L, which makes up the other 10% of the specimen volume. Starting with D_S being equal to D_L, for Case III, D_S was kept at 4 mm and D_L was increased from 4 mm to 12 mm. For Case IV, D_L was kept at 12 mm, and D_S was reduced from 12 mm to 4 mm

(Table 5). All soil specimens have the same porosity of 0.38, under a confining pressure of 150 kPa.

For Case II. Studies considered five soils made up of uniform spherical particles. When increasing the size of the particles from 4 mm to 12 mm, the peak deviatoric stress, internal friction angles, and dilatancy angles—all decreased. The deviatoric stress reduced by almost 37%, and the friction angle decreased from 36.3° to 28.5°. The dilatancy angle decreased from 5.1° to 0° as shown in Fig. 17a and 18a. Thus, for Case II, the three parameters *decrease* with an increasing D_{50}. Conversely, in the previous analysis of Case I for soil with gradation, the specimen's peak deviatoric stress, internal friction angle, and dilatancy angle increased with an increasing D_{50}. The finding from this study that the angle of internal friction *decreases* with the increase of uniform particle size disagrees with a conclusion from Islam et al. (2011), which was based on a series of direct shear tests. They stated that with an increase in particle size, the friction angle *increases* for uniform sands and graded sands (Islam et al. 2011). However, the finding agrees with two older studies by Kirpatric (1965) and Marschi et al. (1972) (Kirkpatric 1965; Marschi et al. 1972). The stance on this issue can be explained by noting the reduction in deviatoric stress and friction angle with the increasing particle sizes. This observation is based on uniform soil with spherical particles, wherein the increasing particle size reduces the number of contact points in the specimens, thereby causing a reduction in the soil's strength.

The fittings of the peak deviatoric stress, internal friction angles, and dilatancy angles as functions of particle size are presented in Figure 18a. The relationships between the three parameters and particle size are inversely linear. These relationships can help predict the changes in the parameters with particle size.

For Case III. The smaller diameter D_S was kept unchanged at 4 mm, and the larger diameter D_L is increased, peak deviatoric stress, internal friction angle, and dilatancy angle all increased. When D_L increased from 4 mm to 12 mm. The deviatoric stress increased 47%, and the friction angle increased from 36.3° to 43.0°. The dilatancy angle increased significantly from 5.1° to 16.0°. This means that for Case III, the three parameters increased with the increasing D_{50}. Direct relationships can be clearly seen between the larger particle size D_L with the deviatoric stress, friction angle, and dilation angle. This is due to the presence of larger particles in the specimen with effects that are as similar to those described in Case I. The fitting obtained in Figure 18b shows the three relationships to be almost linear.

For Case IV. When the larger diameter D_L was kept unchanged, and the smaller diameter D_S was decreased, the deviatoric stresses, friction angle, and dilatancy angle of the soil increased. When D_S decreased from 12 mm to 4 mm, the deviatoric stress increased by more than 120%, the friction angle increased significantly from 28.5° to 43.0°, and the dilatancy angle increased from 0° to 16.0°. Here, the three parameters *decreased* with the increasing D_{50}. This is the reverse relationship similar to Case I. Again, linear relationships were observed between D_S the particles in the 90% volume and the three parameters, which are shown in Figure 18c.

Table 5. Deviatoric Stress, Internal Friction Angle, and Dilatancy Angle

		Diameter	$\Delta\sigma\ (kPa)$	φ (°) at peak	Ψ (°)
Case II: Uniform with	spherical particle diameter of	4 mm	435	36.3	5.1
		6 mm	372	33.6	4.2
		8 mm	338	32.0	2.3
		10 mm	317	30.8	0.9
		12 mm	274	28.5	0
Case III: Gradation of 90%	of 4 mm, and 10 % of	4 mm	435	36.3	5.1
		6 mm	481	38.0	9.6
		8 mm	514	39.2	11.1
		10 mm	613	42.2	15.0
		12 mm	640	43.0	16.0
Case IV: Gradation of 10 %	of 12 mm, and 90% of	4 mm	640	43.0	16.0
		6 mm	540	40.0	12.1
		8 mm	473	37.7	9.2
		10 mm	362	33.1	3.6
		12 mm	274	28.5	0

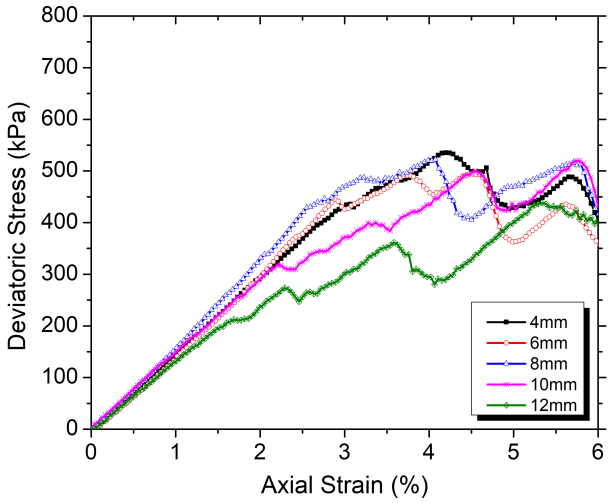

(i) Stress-strain curves.

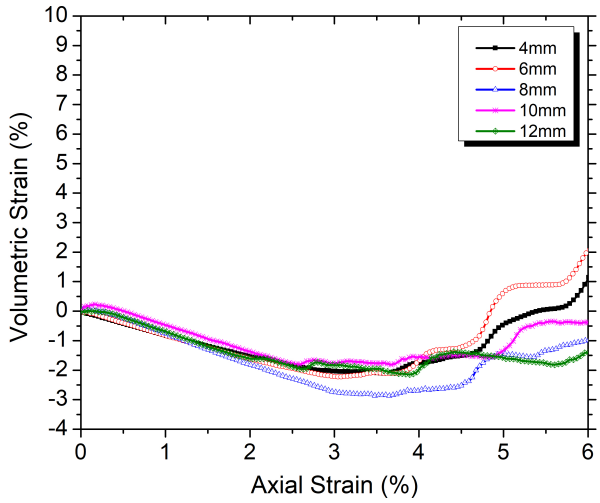

(ii) Volumetric strain.

(a) Case II: Uniform particle size.

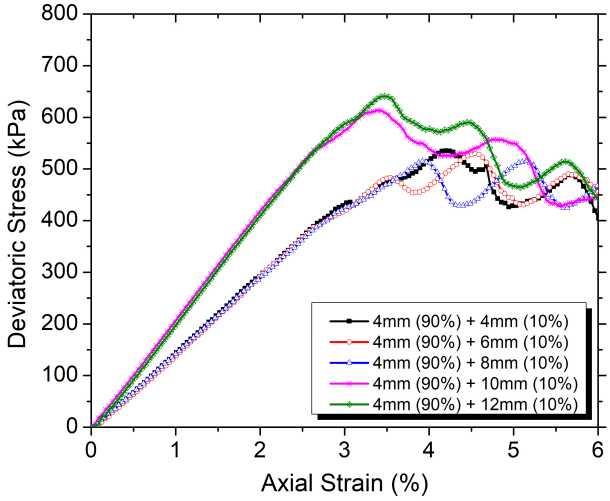

(i) Stress-strain curves.

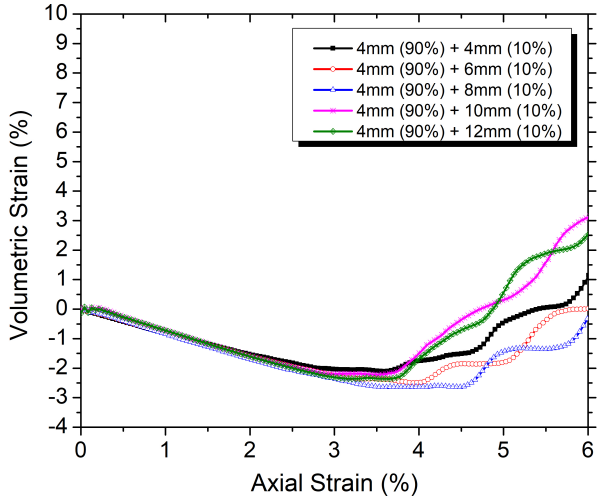

(ii) Volumetric strain.

(b) Case III: 90% volume with 4 mm particle base.

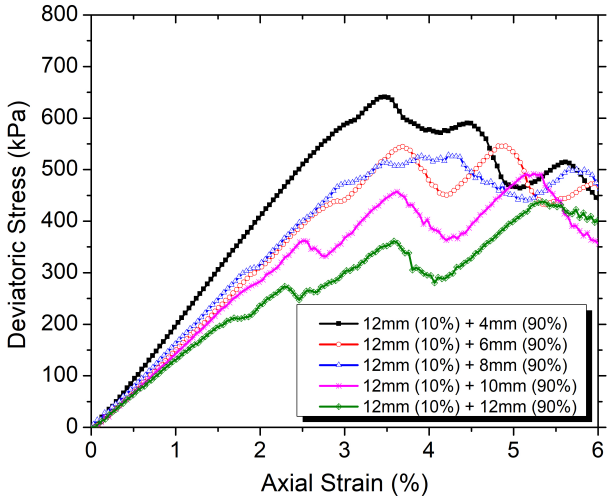

(i) Stress-strain curves.

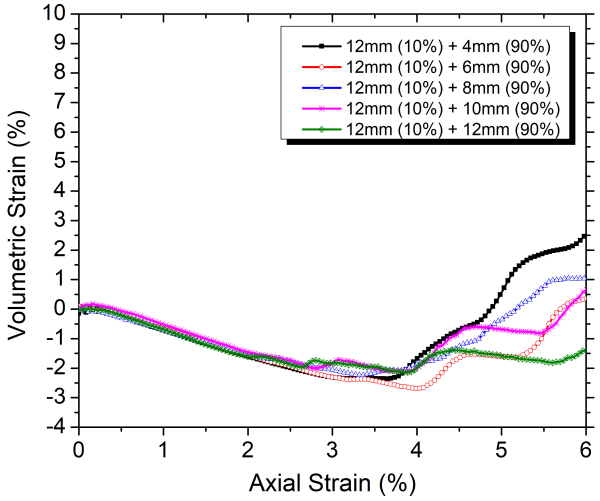

(ii) Volumetric strain.

(c) Case IV: 10% volume with 12 mm particle base.

Figure 17. Stress-strain relation and volume change

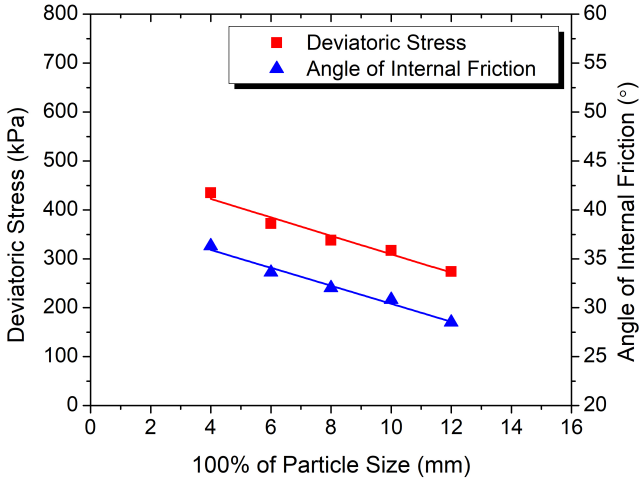

(i) Deviatoric stress and friction angle as a funtion of partical size.

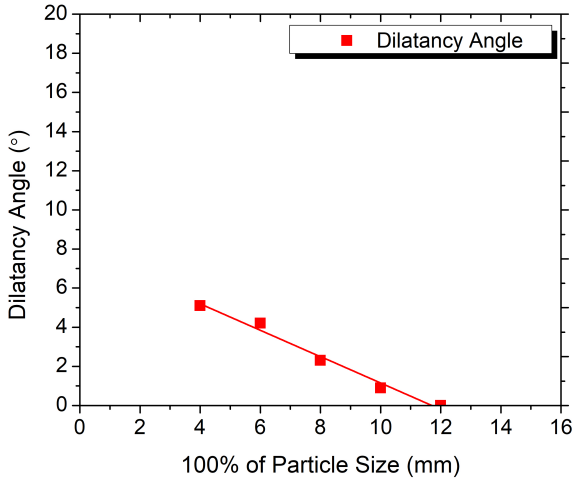

(ii) Dilatancy angle as a funtion of partical size.

(a) Case II: Uniform particle size.

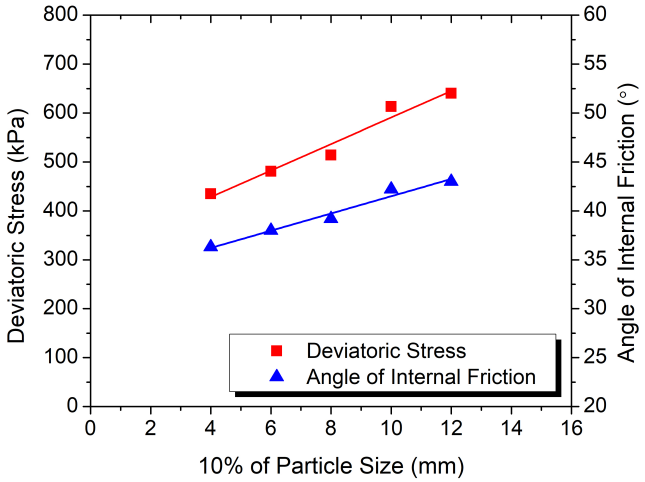

(i) Deviatoric stress and friction angle as a funtion of larger particle size portion.

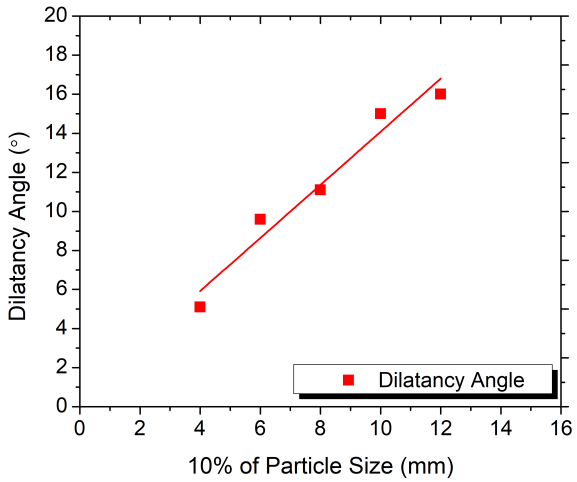

(ii) Dilatancy angle as a funtion of larger particle size portion.

(b) Case III: 90% of 4 mm-particle base mixed with the remaining 10% volume consisting of different size particles.

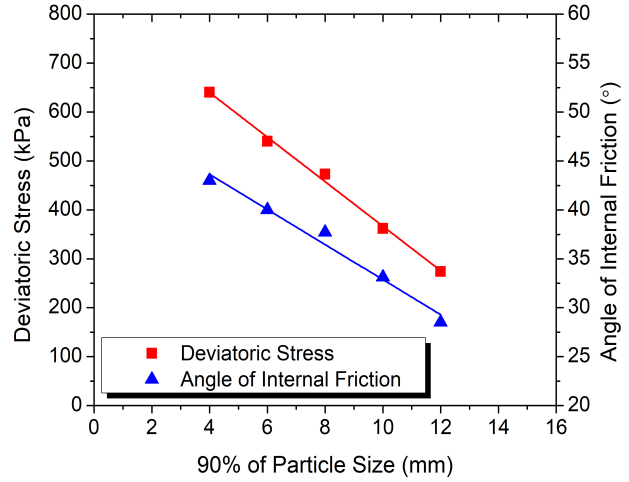

(i) Deviatoric stress and friction angle as a funtion of smaller particle size portion.

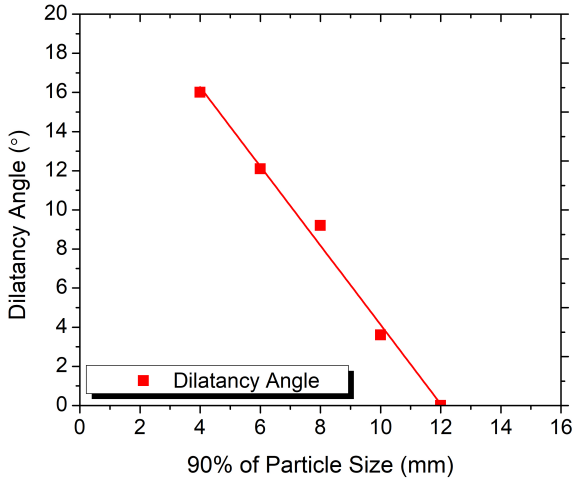

(ii) Dilatancy angle as a funtion of smaller particle size portion.

(c) Case IV: 10% of 12-mm particles base mixed with 90% of different size particles.

Figure 18. Relationship between deviatoric stress, angle of internal friction, and dilatancy angle with particle size.

Among the four cases with different soil gradations, two cases revealed an increase in deviatoric stress, friction angle, and dilatancy angle with a decreasing D_{50}. This is because of the increase in the number of particles and particle contacts within Case II specimen's uniform soil as well as a better particle size distribution when increasing the range of the particle sizes with the presence of larger-diameter particles for Case IV. These conditions make soil stronger and more resilient to shear. Conversely, for the other two cases, where the three parameters increase with an increasing D_{50}, these cases involve a smaller range of particle sizes with a poorer grain size distribution, which makes the soil weaker. The finding of linear relationship in the deviatoric stresses, friction angle, and dilatancy angle based on particle size is significant since it can help predict soil strength and strain properties when the particle size changes.

Observations on Shear Bands

In a laboratory triaxial test, it is difficult to observe the weakest plane in a specimen during shear failure or "shear band." The developed DEM model for the triaxial test with a flexible membrane is able to track the shear band during failure. As the granular specimen transmits external forces, internal force chains continuously break and reform (Wilson and Sáez 2017); thus, the weakest internal forces during shear failure can be traced. A shear band can be tracked by either tracing particle movements or tracing the internal forces in the discrete granular medium. Shear band is more visible and more band-like for the higher confining stress σ_3 of 150 KPa than for the lower σ_3.

To observe and compare the development of the shear bands for different particle sizes and confining pressures, triaxial tests on two specimens with a uniform particle size of 4 mm and 8 mm were simulated at three confining pressures. Both specimens generated almost slant band-

like shear zones. Figure 19 shows the specimen with 4 mm particles possessing a comparatively thinner shear band area, and the specimen with 8 mm particles possessing a thicker shear band area. The thicker shear band for larger particles may come from the interaction of larger particles when the specimen has a larger area of the specimen involved in the shear band. The movement of the particles on the shear surface also seems larger for large particles as shown by the differences between Fig. 19c and 19f.

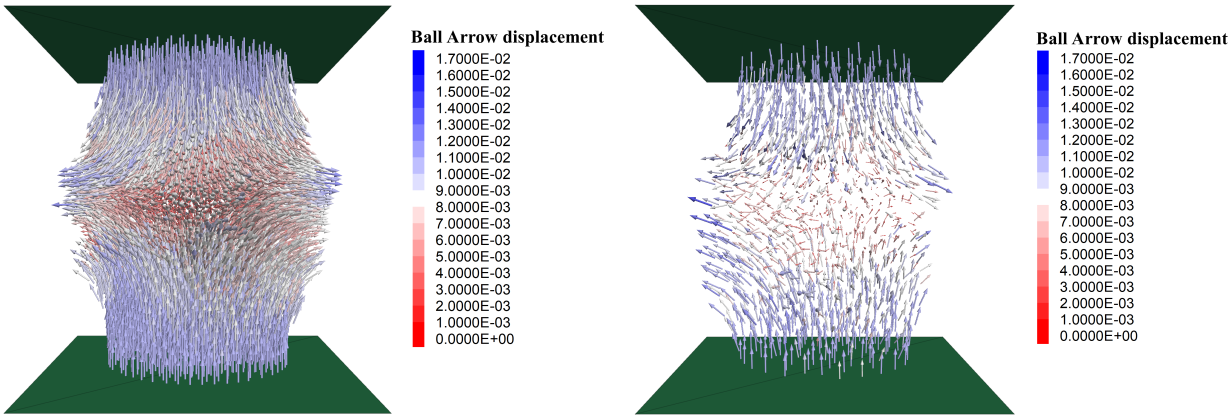

(a) Specimen with 4 mm particles, σ_3=35 kPa (d) Specimen with 8 mm particles, σ_3=35 kPa

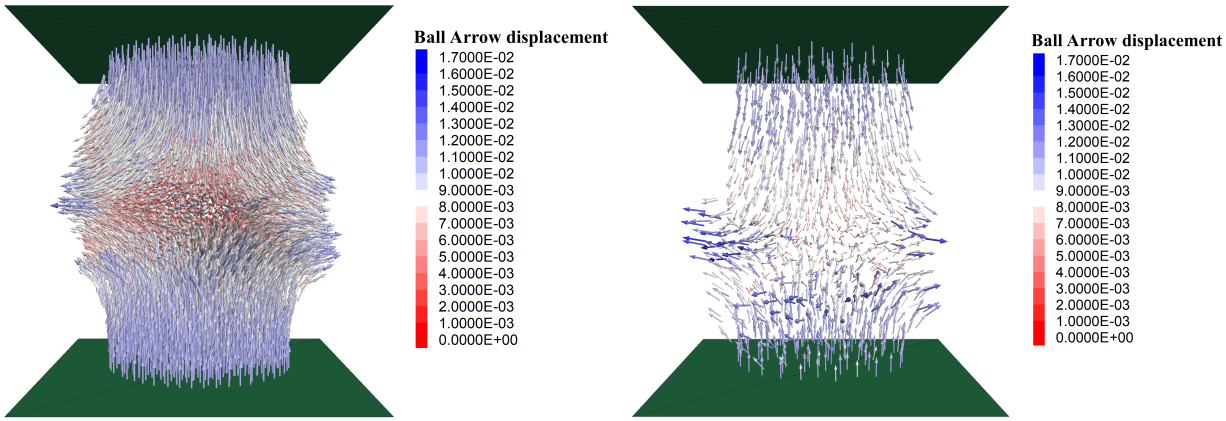

(b) Specimen with 4 mm particles, σ_3=70 kPa (e) Specimen with 8 mm particles, σ_3=70 kPa

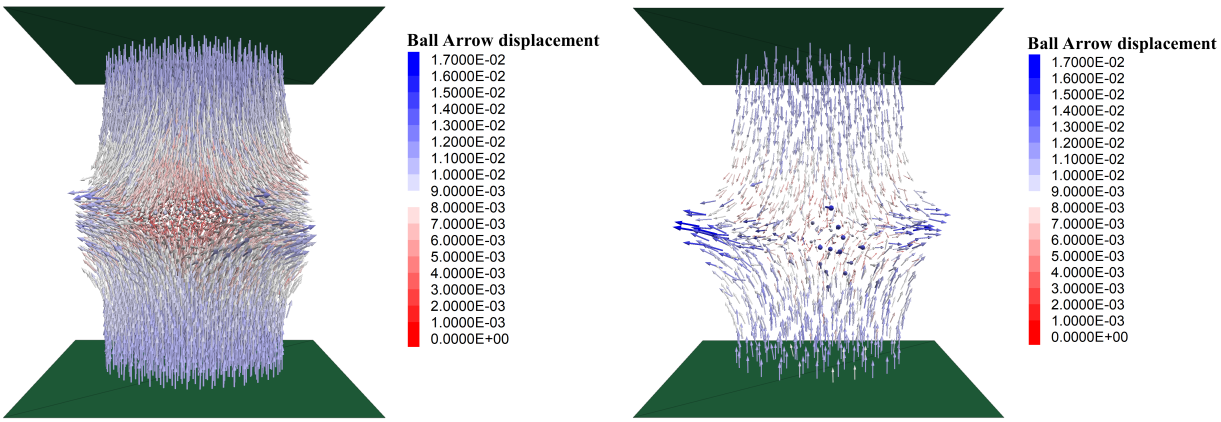

(c) Specimen with 4 mm particles, σ_3=150 kPa (f) Specimen with 8 mm particles, σ_3=150 kPa

Figure 19. Shear bands during failure

The 3D DEM model enables predictions of behavioral characteristics in granular soil. For future study, Geosynthetics will be added to the specimen to study the stress-strain behaviors of reinforced soil in a mechanically stabilized earth (MSE) retaining wall or a geosynthetic reinforced soil (GRS) mass, which will have important applications that can improve the design of these structures.

Reinforced VS Unreinforced Specimen

Specimen size is increased to five times and other micro-parameters are adjusted accordingly. One geogrid layered reinforced triaxial specimens are compared with unreinforced specimens at different confining pressures of 35, 70, 150 kPa. It is obvious from the stress-strain plot (Figure 20) that reinforced specimens have higher shear strength than the unreinforced specimens. From the Mohr coulomb analysis (Figure. 21), it is found that angle of internal friction (φ_{soil}) is 35.5° for the cohesionless soil.

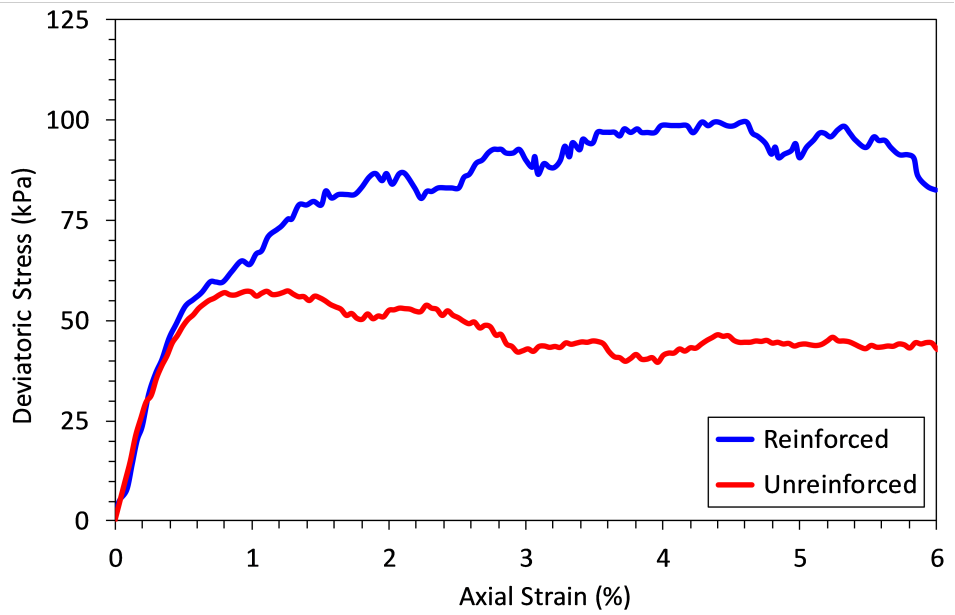

(a) Confining pressure = 35 kPa

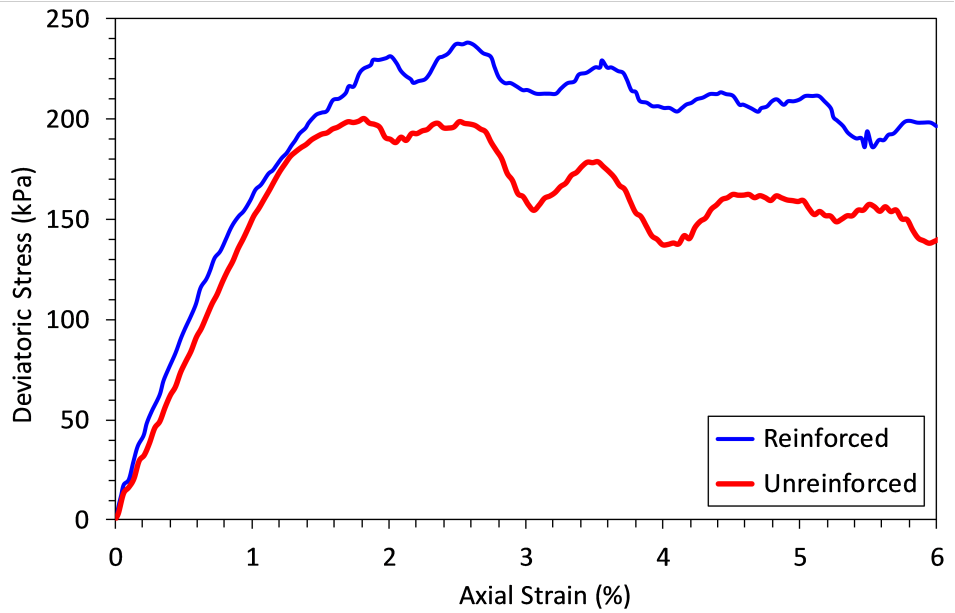

(b) Confining pressure = 70 kPa

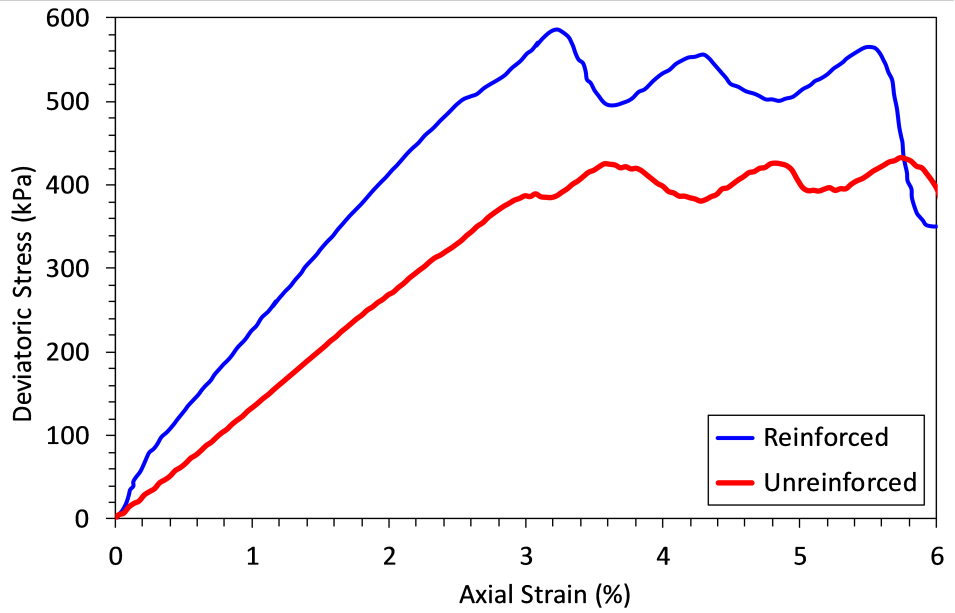

(c) Confining pressure = 150 kPa

Figure 20. Comparison of stress-strain curves for reinforced and unreinforced specimen at different confining pressure

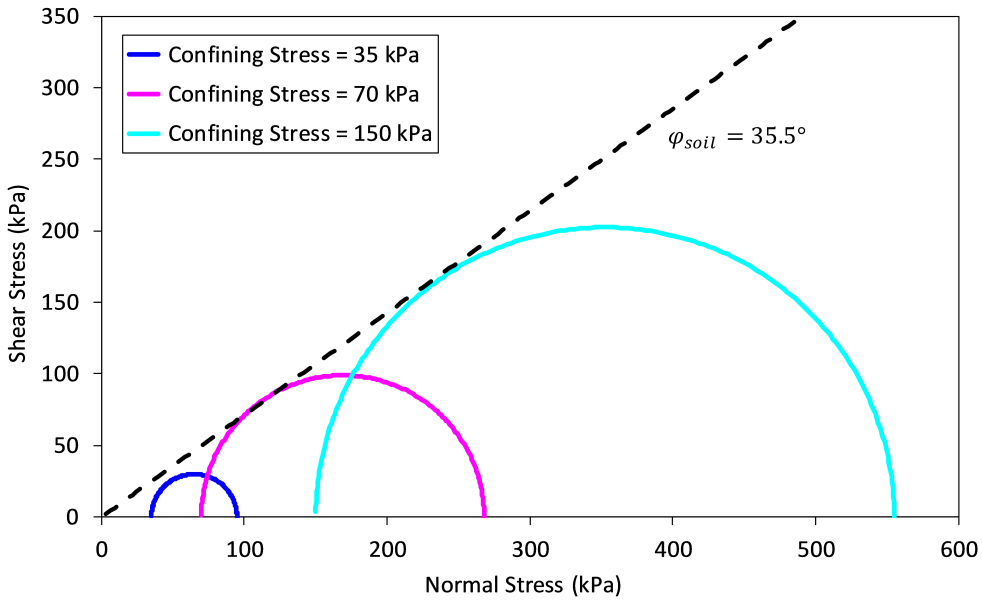

Figure 21. Mohr's Circles generated for unreinforced specimen to obtain C and φ

One Geogrid Layer

A single layer of geogrid is embedded at the middle of the specimen. From the Mohr coulomb analysis (Figure. 22), it is found that reinforced cohesion (C_R) is 1 kPa and reinforced angle of internal friction (φ_R) is 35.5° which is same as the friction angle of soil in unreinforced specimen (φ_{soil}). It is observed that even only a single layer of geogrid helps adding cohesion to the granular specimen, however, the internal friction angle is found similar as unreinforced soil specimen.

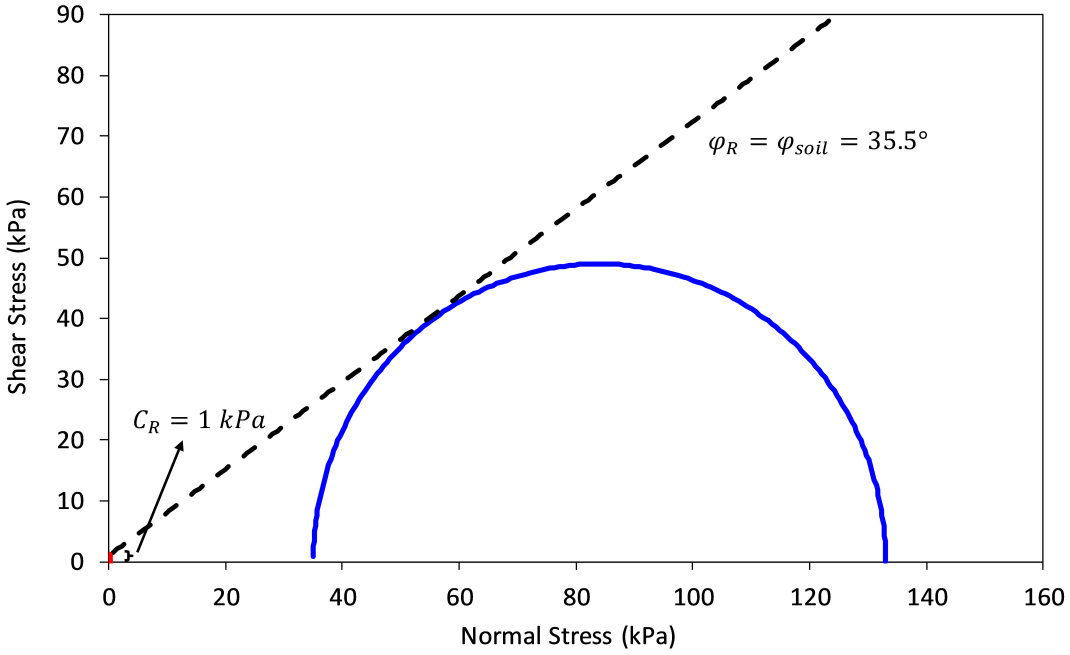

Figure 22. Mohr's Circles generated for reinforced specimen to obtain $C\ and\ \varphi$ at 35 kPa confining pressure.

Grid Displacement

Grid displacement has been observed for one geogrid layer model. Grid particles that are close to boundary has faced maximum displacement (Figure 23). Reinforcement does not break for the high strength geogrid, so, weaker geogrid with low effective modulus ($E^* = 5e^3\ Pa$) and stiffness ratio ($k^* = 1.5$) is used in this study to observe the reinforcement failure and the overall specimen shear failure surface. However, the model confirms that geogrid plays greater role and needs more attention during design of the Mechanically Stabilized Earth (MSE) wall or Geosynthetic Reinforced Soil (GRS) structures.

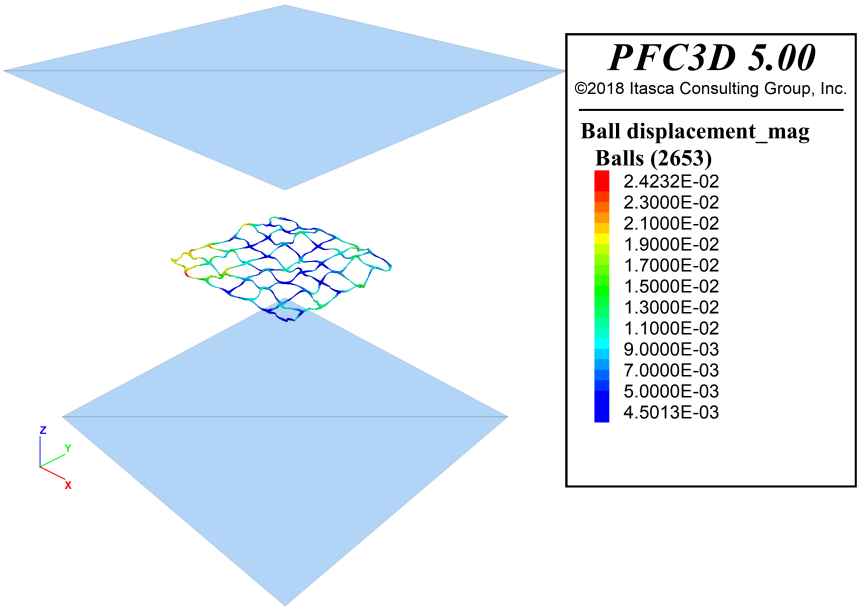

(a) one geogrid layer

Figure 23. Geogrid displacement for one geogrid layer at the end of triaxial shearing

In a laboratory triaxial test, it is difficult to observe the weakest plane in a specimen during shear failure or "shear band." The developed DEM model for the reinforced triaxial test with a flexible membrane can track the shear band during failure (Figure 24). Shear band is visible even at low confining pressure ($\sigma_3 = 35\ kPa$) and supposed to form a clearer band-like distribution at the higher confining pressure.

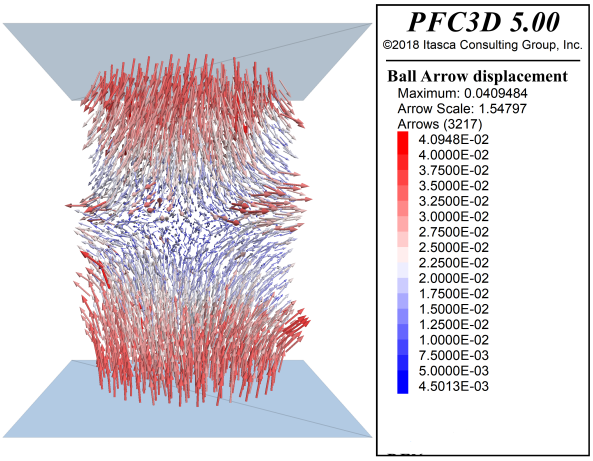

Figure 24. Reinforced specimen displacement at the end of triaxial shearing

CHAPTER VI

CONCLUSIONS

A 3D DEM model was developed using PFC, utilizing a bonded-ball flexible membrane approach to study the strength and strain properties of cohesionless soils as a discontinuous discrete material. Sensitivity analyses were carried out for the microparameters as inputs for the 3D model, which led to the finding that an increase in particle normal stiffness and shear stiffness increases the material elastic modulus. The change of normal and shear stiffness, however, does not affect the peak strength of the soils. Besides, increasing friction coefficient causes an increase in peak strength, but does not affect either the material elastic modulus or the residual stresses of the stress-strain curves. A series of triaxial tests with flexible membranes were simulated to obtain the stress-strain behaviors of granular soil specimens. Four different cases were studied to investigate the effects of particle size and gradation on soil strength and strain properties. Increasing the maximum particle size for soil with gradation gives rise to the strength, the internal friction angle, and the angle of dilatancy, meaning these three parameters increase when increasing the mean particle size D_{50}. However, these three factors do not always increase when the mean particle size D_{50} increases but depend instead on the gradations. The relationships between particle size and deviatoric stress, internal friction angle, and dilatancy angle were found to be linear. These linear relationships can provide predictions on soil strength and strain properties when particle sizes change. The developed model with a bonded-ball flexible membrane that allows the study of soil as a discrete material also allows the observance

of shear band formation during shear testing. It also shows that developed flexible membrane model can capture the stress-strain response of the geogrid specimen well. The model proves that apparent cohesion may develop to the cohesionless specimen that increases the shear strength of the specimen. The developed model and the findings from this research create the foundation for the future research on DEM modeling of reinforced soil in MSE wall and GRS mass.

REFERENCES

Abu-Hassan, Mohammad. 2006. “Anisotropic Elastic Modeling of Reinforced Soil.” Ph.D. Thesis, University of Colorado, Denver.

Addenbrooke, T. I., D. M. Potts, and A. M. Puzrin. 1997. “The Influence of Pre-Failure Soil Stiffness on the Numerical Analysis of Tunnel Construction.” *Géotechnique* 47(3):693–712. doi: 10.1680/geot.1997.47.3.693.

Ahlinhan, Marx Ferdinand, Ernesto Houehanou, Marius Bocco Koube, Valery Doko, Quirin Alaye, Nicholas Sungura, and Edmond Adjovi. 2018. “Experiments and 3D DEM of Triaxial Compression Tests under Special Consideration of Particle Stiffness.” *Geomaterials* 08(04):39–62. doi: 10.4236/gm.2018.84004.

Ahmadi, Hamzeh, and Adam Bezuijen. 2018. “Full-Scale Mechanically Stabilized Earth (MSE) Walls under Strip Footing Load.” *Geotextiles and Geomembranes* 46(3):297–311. doi: 10.1016/j.geotexmem.2017.12.002.

Alamshahi, Saeed, and Nader Hataf. 2009. “Bearing Capacity of Strip Footings on Sand Slopes Reinforced with Geogrid and Grid-Anchor.” *Geotextiles and Geomembranes* 27(3):217–26. doi: 10.1016/j.geotexmem.2008.11.011.

Allen, T. M., and R. J. Bathurst. 2002. “Observed Long-Term Performance of Geosynthetic Walls and Implications for Design.” *Geosynthetics International* 9(5–6):567–606. doi: 10.1680/gein.9.0228.

Amirpour Harehdasht, Samaneh, Mourad Karray, Mahmoud N. Hussien, and Mohamed Chekired. 2017. “Influence of Particle Size and Gradation on the Stress-Dilatancy Behavior of Granular Materials during Drained Triaxial Compression.” *International Journal of Geomechanics* 17(9):04017077. doi: 10.1061/(ASCE)GM.1943-5622.0000951.

Bagherzadeh-Khalkhali, Ahad, and Ali Asghar Mirghasemi. 2009. “Numerical and Experimental Direct Shear Tests for Coarse-Grained Soils.” *Particuology* 7(1):83–91. doi: 10.1016/j.partic.2008.11.006.

Bardet, J. P., and J. Proubet. 1991. “A Numerical Investigation of the Structure of Persistent Shear Bands in Granular Media.” *Géotechnique* 41(4):599–613. doi: 10.1680/geot.1991.41.4.599.

Bathurst, R. J., and F. M. Ezzein. 2016. “Geogrid Pullout Load–Strain Behaviour and Modelling Using a Transparent Granular Soil.” *Geosynthetics International* 23(4):271–86. doi: 10.1680/jgein.15.00051.

Bathurst, R. J., and F. M. Ezzein. 2017. “Insights into Geogrid–Soil Interaction Using a Transparent Granular Soil.” *Géotechnique Letters* 7(2):179–83. doi: 10.1680/jgele.16.00191.

Bathurst, Richard J., and Fawzy M. Ezzein. 2015. “Geogrid and Soil Displacement Observations During Pullout Using a Transparent Granular Soil.” *Geotechnical Testing Journal* 38(5):20140145. doi: 10.1520/GTJ20140145.

Bathurst, Richard J., and Gerald P. Raymond. 1987. *Reinforced Layered Systems*. Transportation Research Board.

Belheine, N., J. P. Plassiard, F. V. Donzé, F. Darve, and A. Seridi. 2009. “Numerical Simulation of Drained Triaxial Test Using 3D Discrete Element Modeling.” *Computers and Geotechnics* 36(1):320–31. doi: 10.1016/j.compgeo.2008.02.003.

Ben-David, Oded, Shmuel M. Rubinstein, and Jay Fineberg. 2010. “Slip-Stick and the Evolution of Frictional Strength.” *Nature* 463(7277):76–79. doi: 10.1038/nature08676.

Benjamim, C. V. S., B. S. Bueno, and J. G. Zornberg. 2007. “Field Monitoring Evaluation of Geotextile-Reinforced Soil-Retaining Walls.” *Geosynthetics International* 14(2):100–118. doi: 10.1680/gein.2007.14.2.100.

Bergado, D. T., P. V. Long, C. H. Lee, K. H. Loke, and G. Werner. 1994. “Performance of Reinforced Embankment on Soft Bangkok Clay with High-Strength Geotextile Reinforcement.” *Geotextiles and Geomembranes* 13(6–7):403–20. doi: 10.1016/0266-1144(94)90005-1.

Bhandari, Anil, and Jie Han. 2010. “Investigation of Geotextile–Soil Interaction under a Cyclic Vertical Load Using the Discrete Element Method.” *Geotextiles and Geomembranes* 28(1):33–43. doi: 10.1016/j.geotexmem.2009.09.005.

Binesh, Seyed Mohammad, Ehsan Eslami-Feizabad, and Reza Rahmani. 2018. “Discrete Element Modeling of Drained Triaxial Test: Flexible and Rigid Lateral Boundaries.” *International Journal of Civil Engineering* 16(10):1463–74. doi: 10.1007/s40999-018-0293-0.

Bolton, M. D. 1986. “The Strength and Dilatancy of Sands.” *Géotechnique* 36(1):65–78. doi: 10.1680/geot.1986.36.1.65.

de Bono, J., G. Mcdowell, and D. Wanatowski. 2012. “Discrete Element Modelling of a Flexible Membrane for Triaxial Testing of Granular Material at High Pressures.” *Géotechnique Letters* 2(4):199–203. doi: 10.1680/geolett.12.00040.

de Bono, J. P., and G. R. McDowell. 2014. “DEM of Triaxial Tests on Crushable Sand.” *Granular Matter* 16(4):551–62. doi: 10.1007/s10035-014-0500-x.

Brown, S. F., J. Kwan, and N. H. Thom. 2007. “Identifying the Key Parameters That Influence Geogrid Reinforcement of Railway Ballast.” *Geotextiles and Geomembranes* 25(6):326–35. doi: 10.1016/j.geotexmem.2007.06.003.

Cardile, G., D. Gioffrè, N. Moraci, and L. S. Calvarano. 2017. "Modelling Interference between the Geogrid Bearing Members under Pullout Loading Conditions." *Geotextiles and Geomembranes* 45(3):169–77. doi: 10.1016/j.geotexmem.2017.01.008.

Chen, Cheng, G. R. McDowell, and N. H. Thom. 2012. "Discrete Element Modelling of Cyclic Loads of Geogrid-Reinforced Ballast under Confined and Unconfined Conditions." *Geotextiles and Geomembranes* 35:76–86. doi: 10.1016/j.geotexmem.2012.07.004.

Chen, Jian-Feng, and Song-Bo Yu. 2011. "Centrifugal and Numerical Modeling of a Reinforced Lime-Stabilized Soil Embankment on Soft Clay with Wick Drains." *International Journal of Geomechanics* 11(3):167–73. doi: 10.1061/(ASCE)GM.1943-5622.0000045.

Chen, Wei-Bin, Wan-Huan Zhou, and Jaime Alberto dos Santos. 2020. "Analysis of Consistent Soil–Structure Interface Response in Multi–Directional Shear Tests by Discrete Element Modeling." *Transportation Geotechnics* 24:100379. doi: 10.1016/j.trgeo.2020.100379.

Cheng, Hongyang, Haruyuki Yamamoto, Klaus Thoeni, and Yang Wu. 2017. "An Analytical Solution for Geotextile-Wrapped Soil Based on Insights from DEM Analysis." *Geotextiles and Geomembranes* 45(4):361–76. doi: 10.1016/j.geotexmem.2017.05.001.

Cheung, Geraldine, and Catherine O'Sullivan. 2008. "Effective Simulation of Flexible Lateral Boundaries in Two- and Three-Dimensional DEM Simulations." *Particuology* 6(6):483–500. doi: 10.1016/j.partic.2008.07.018.

Cil, Mehmet B., and Khalid A. Alshibli. 2014. "3D Analysis of Kinematic Behavior of Granular Materials in Triaxial Testing Using DEM with Flexible Membrane Boundary." *Acta Geotechnica* 9(2):287–98. doi: 10.1007/s11440-013-0273-0.

Coetzee, C. J. 2016. "Calibration of the Discrete Element Method and the Effect of Particle Shape." *Powder Technology* 297:50–70. doi: 10.1016/j.powtec.2016.04.003.

Coetzee, C. J. 2017. "Review: Calibration of the Discrete Element Method." *Powder Technology* 310:104–42. doi: 10.1016/j.powtec.2017.01.015.

Coetzee, C. J., and D. N. J. Els. 2009. "Calibration of Discrete Element Parameters and the Modelling of Silo Discharge and Bucket Filling." *Computers and Electronics in Agriculture* 65(2):198–212. doi: 10.1016/j.compag.2008.10.002.

Cundall, P. A., and O. D. L. Strack. 1979. "A Discrete Numerical Model for Granular Assemblies." *Géotechnique* 29(1):47–65. doi: 10.1680/geot.1979.29.1.47.

Cundall, PETER A., and ROGER D. Hart. 1993. "Numerical Modeling of Discontinua." Pp. 231–43 in *Analysis and Design Methods*, edited by C. Fairhurst. Oxford: Pergamon.

Dai, Bei Bing, Jun Yang, and Cui Ying Zhou. 2016. "Observed Effects of Interparticle Friction and Particle Size on Shear Behavior of Granular Materials." *International Journal of Geomechanics* 16(1):04015011. doi: 10.1061/(ASCE)GM.1943-5622.0000520.

Demir, Ahmet, Mustafa Laman, Abdulazim Yildiz, and Murat Ornek. 2013. “Large Scale Field Tests on Geogrid-Reinforced Granular Fill Underlain by Clay Soil.” *Geotextiles and Geomembranes* 38:1–15. doi: 10.1016/j.geotexmem.2012.05.007.

Effeindzourou, Anna, Klaus Thoeni, Anna Giacomini, and Corinna Wendeler. 2017. “Efficient Discrete Modelling of Composite Structures for Rockfall Protection.” *Computers and Geotechnics* 87:99–114. doi: 10.1016/j.compgeo.2017.02.005.

El Sawwaf, Mostafa A. 2007. “Behavior of Strip Footing on Geogrid-Reinforced Sand over a Soft Clay Slope.” *Geotextiles and Geomembranes* 25(1):50–60. doi: 10.1016/j.geotexmem.2006.06.001.

Esmaeili, Morteza, Jabbar Ali Zakeri, and Mohammad Babaei. 2017. “Laboratory and Field Investigation of the Effect of Geogrid-Reinforced Ballast on Railway Track Lateral Resistance.” *Geotextiles and Geomembranes* 45(2):23–33. doi: 10.1016/j.geotexmem.2016.11.003.

Ezzein, Fawzy M., and Richard J. Bathurst. 2014. “A New Approach to Evaluate Soil-Geosynthetic Interaction Using a Novel Pullout Test Apparatus and Transparent Granular Soil.” *Geotextiles and Geomembranes* 42(3):246–55. doi: 10.1016/j.geotexmem.2014.04.003.

Ferreira, F. B., A. Topa Gomes, C. S. Vieira, and M. L. Lopes. 2016. “Reliability Analysis of Geosynthetic-Reinforced Steep Slopes.” *Geosynthetics International* 23(4):301–15. doi: 10.1680/jgein.15.00057.

Frost, J. David, and T. Matthew Evans. 2009. “Membrane Effects in Biaxial Compression Tests.” *Journal of Geotechnical and Geoenvironmental Engineering* 135(7):986–91. doi: 10.1061/(ASCE)GT.1943-5606.0000011.

Gao, Ge, and M. A. Meguid. 2018. “On the Role of Sphericity of Falling Rock Clusters—Insights from Experimental and Numerical Investigations.” *Landslides* 15(2):219–32. doi: 10.1007/s10346-017-0874-z.

Griffiths, D. V., and G. G. W. Mustoe. 2001. “Modelling of Elastic Continua Using a Grillage of Structural Elements Based on Discrete Element Concepts.” *International Journal for Numerical Methods in Engineering* 50(7):1759–75. doi: 10.1002/nme.99.

Gupta, Ashok Kumar. 2016. “Effects of Particle Size and Confining Pressure on Breakage Factor of Rockfill Materials Using Medium Triaxial Test.” *Journal of Rock Mechanics and Geotechnical Engineering* 8(3):378–88. doi: 10.1016/j.jrmge.2015.12.005.

Henkel, D. J., and G. D. Gilbert. 1952. “The Effect Measured of the Rubber Membrane on the Triaxial Compression Strength of Clay Samples.” *Géotechnique* 3(1):20–29. doi: 10.1680/geot.1952.3.1.20.

Holtz, R. D. 2017. “46th Terzaghi Lecture: Geosynthetic Reinforced Soil: From the Experimental to the Familiar.” *Journal of Geotechnical and Geoenvironmental Engineering* 143(9):03117001. doi: 10.1061/(ASCE)GT.1943-5606.0001674.

Hussein, M. G., and M. A. Meguid. 2016. “A Three-Dimensional Finite Element Approach for Modeling Biaxial Geogrid with Application to Geogrid-Reinforced Soils.” *Geotextiles and Geomembranes* 44(3):295–307. doi: 10.1016/j.geotexmem.2015.12.004.

Indraratna, B., H. Khabbaz, W. Salim, and D. Christie. 2006. “Geotechnical Properties of Ballast and the Role of Geosynthetics in Rail Track Stabilisation.” *Proceedings of the Institution of Civil Engineers - Ground Improvement* 10(3):91–101. doi: 10.1680/grim.2006.10.3.91.

Islam, M. N., A. Siddika, M. B. Hossain, A. Rahman, and M. A. Asad. 2011. “Effect of Particle Size on the Shear Strength Behavior of Sands.” *Australian Geomechanics Journal* 46(3):75–86.

Itasca. 2014. “Particle Flow Code in Three Dimensions.”

Iwashita Kazuyoshi, and Oda Masanobu. 1998. “Rolling Resistance at Contacts in Simulation of Shear Band Development by DEM.” *Journal of Engineering Mechanics* 124(3):285–92. doi: 10.1061/(ASCE)0733-9399(1998)124:3(285).

Jacobs, Felix, and Martin Ziegler. 2016. “Investigation of Global Stress-Strain and Interaction Behavior of Geogrid Reinforced Soil with Biaxial Compression Tests.” *Japanese Geotechnical Society Special Publication* 2(65):2209–14. doi: 10.3208/jgssp.IGS-32.

Javankhoshdel, S., and R. J. Bathurst. 2017. “Deterministic and Probabilistic Failure Analysis of Simple Geosynthetic Reinforced Soil Slopes.” *Geosynthetics International* 24(1):14–29. doi: 10.1680/jgein.16.00012.

Jiang, Mingjing, Tao Li, and Zhifu Shen. 2016. “Fabric Rates of Elliptical Particle Assembly in Monotonic and Cyclic Simple Shear Tests: A Numerical Study.” *Granular Matter* 18(3):54. doi: 10.1007/s10035-016-0641-1.

Keskin, M. Salih, and Mustafa Laman. 2014. “Experimental and Numerical Studies of Strip Footings on Geogrid-Reinforced Sand Slope.” *Arabian Journal for Science and Engineering* 39(3):1607–19. doi: 10.1007/s13369-013-0795-7.

Ketchart, K., and J. T. H. Wu. 1996. *Long-Term Performance Tests of Soil-Geosynthetic Composites*. CDOTCTI-96-1. Denver: Colorado Department of Transportation.

Khoubani, Ali, and T. Matthew Evans. 2018. “An Efficient Flexible Membrane Boundary Condition for DEM Simulation of Axisymmetric Element Tests.” *International Journal for Numerical and Analytical Methods in Geomechanics* 42(4):694–715. doi: 10.1002/nag.2762.

Kim, D., and S. Ha. 2014. “Effects of Particle Size on the Shear Behavior of Coarse-Grained Soils Reinforced with Geogrid.” 7(2):963–979. doi: https://dx.doi.org/10.3390%2Fma7020963.

Kim, Daehyeon, Myung Sagong, and Yonghee Lee. 2005. “Effects of Fine Aggregate Content on the Mechanical Properties of the Compacted Decomposed Granitic Soils.” *Construction and Building Materials* 19(3):189–96. doi: 10.1016/j.conbuildmat.2004.06.002.

Kirkpatric, W. M. 1965. “Effects of Grain Size and Grading on the Shearing Behavior of Granular Materials.” Pp. 273–77 in *Proceedings of the 6th International Conference on Soil Mechanics and Foundation Engineering*. Vol. 1. Canada.

Kishino, Y. 1988. “Disc Model Analysis of Granular Media.” Pp. 143–52 in *Studies in Applied Mechanics*. Vol. 20. Elsevier.

Kongkitkul, Warat, Daiki Hirakawa, Fumio Tatsuoka, and Taro Kanemaru. 2007. “Effects of Geosynthetic Reinforcement Type on the Strength and Stiffness of Reinforced Sand in Plane Strain Compression.” *Soils and Foundations* 47(6):1109–22. doi: 10.3208/sandf.47.1109.

Kongkitkul, Warat, Fumio Tatsuoka, and Daiki Hirakawa. 2007. “Rate-Dependent Load-Strain Behaviour of Geogrid Arranged in Sand Under Plane Strain Compression.” *Soils and Foundations* 47(3):473–91. doi: 10.3208/sandf.47.473.

Kozicki, J., and J. Tejchman. 2016. “DEM Investigations of Two-Dimensional Granular Vortex- and Anti-Vortex-Structures during Plane Strain Compression.” *Granular Matter* 18(2):20. doi: 10.1007/s10035-016-0627-z.

Kuhn, Matthew R. 1995. “A Flexible Boundary for Three-dimensional Dem Particle Assemblies.” *Engineering Computations* 12(2):175–83. doi: 10.1108/02644409510799541.

Kumar, Jyant, and Jagdish Prasad Sahoo. 2013. “Bearing Capacity of Strip Foundations Reinforced with Geogrid Sheets by Using Upper Bound Finite-Element Limit Analysis: BEARING CAPACITY OF REINFORCED FOUNDATIONS.” *International Journal for Numerical and Analytical Methods in Geomechanics* 37(18):3258–77. doi: 10.1002/nag.2189.

Lai, Zhengshou, and Qiushi Chen. 2017. “Characterization and Discrete Element Simulation of Grading and Shape-Dependent Behavior of JSC-1A Martian Regolith Simulant.” *Granular Matter* 19(4):69. doi: 10.1007/s10035-017-0754-1.

Li, Bo, Fengshou Zhang, and Marte Gutierrez. 2015. “A Numerical Examination of the Hollow Cylindrical Torsional Shear Test Using DEM.” *Acta Geotechnica* 10(4):449–67. doi: 10.1007/s11440-014-0329-9.

Li, Fu-Lin, Fang-Le Peng, Yong Tan, W. Kongkitkul, and M. S. A. Siddiquee. 2012. “FE Simulation of Viscous Behavior of Geogrid-Reinforced Sand under Laboratory-Scale

Plane-Strain-Compression Testing." *Geotextiles and Geomembranes* 31:72–80. doi: 10.1016/j.geotexmem.2011.09.005.

Lin, Honglin, and Jianhong Zhang. 2016. "Triaxial Tests and DEM Simulation on Artificial Bonded Granular Materials." *Japanese Geotechnical Society Special Publication* 2(17):660–63. doi: 10.3208/jgssp.CHN-05.

Lin, Y. L., M. X. Zhang, A. A. Javadi, Y. Lu, and S. L. Zhang. 2013. "Experimental and DEM Simulation of Sandy Soil Reinforced with H–V Inclusions in Plane Strain Tests." *Geosynthetics International* 20(3):162–73. doi: 10.1680/gein.13.00009.

Ling, Hoe I., and Huabei Liu. 2009. "Deformation Analysis of Reinforced Soil Retaining Walls—Simplistic versus Sophisticated Finite Element Analyses." *Acta Geotechnica* 4(3):203–13. doi: 10.1007/s11440-009-0091-6.

Lommen, Stef, Dingena Schott, and Gabriel Lodewijks. 2014. "DEM Speedup: Stiffness Effects on Behavior of Bulk Material." *Particuology* 12:107–12. doi: 10.1016/j.partic.2013.03.006.

Lu, Ye, Xiaojiao Li, and Yuelin Wang. 2018. "Application of a Flexible Membrane to DEM Modelling of Axisymmetric Triaxial Compression Tests on Sands." *European Journal of Environmental and Civil Engineering* 22(sup1):s19–36. doi: 10.1080/19648189.2018.1425157.

Marigo, Michele, and Edmund Hugh Stitt. 2015. "Discrete Element Method (DEM) for Industrial Applications: Comments on Calibration and Validation for the Modelling of Cylindrical Pellets." *KONA Powder and Particle Journal* 32(0):236–52. doi: 10.14356/kona.2015016.

Marschi, N. Dean, Clarence K. Chan, and H. Bolton Seed. 1972. "Evaluation of Properties of Rockfill Materials." 98(1):95–114.

McDowell, G. R., O. Harireche, H. Konietzky, S. F. Brown, and N. H. Thom. 2006. "Discrete Element Modelling of Geogrid-Reinforced Aggregates." *Proceedings of the Institution of Civil Engineers - Geotechnical Engineering* 159(1):35–48. doi: 10.1680/geng.2006.159.1.35.

Miao, Chen-xi, Jun-jie Zheng, Rong-jun Zhang, and Lan Cui. 2017. "DEM Modeling of Pullout Behavior of Geogrid Reinforced Ballast: The Effect of Particle Shape." *Computers and Geotechnics* 81:249–61. doi: 10.1016/j.compgeo.2016.08.028.

Mishra, Debakanta, and S. M. Naziur Mahmud. 2017. "Effect of Particle Size and Shape Characteristics on Ballast Shear Strength: A Numerical Study Using the Direct Shear Test." P. V001T01A014 in *Joint Rail Conference*. Philadelphia, Pennsylvania, USA: American Society of Mechanical Engineers.

Mishra, Debakanta, Yu Qian, Hasan Kazmee, and Erol Tutumluer. 2014. "Investigation of Geogrid-Reinforced Railroad Ballast Behavior Using Large-Scale Triaxial Testing and

Discrete Element Modeling." *Transportation Research Record: Journal of the Transportation Research Board* 2462(1):98–108. doi: 10.3141/2462-12.

Moraci, N., and P. Recalcati. 2006. "Factors Affecting the Pullout Behaviour of Extruded Geogrids Embedded in a Compacted Granular Soil." *Geotextiles and Geomembranes* 24(4):220–42. doi: 10.1016/j.geotexmem.2006.03.001.

Mosallanezhad, M., S. H. Sadat Taghavi, N. Hataf, and M. C. Alfaro. 2016. "Experimental and Numerical Studies of the Performance of the New Reinforcement System under Pull-out Conditions." *Geotextiles and Geomembranes* 44(1):70–80. doi: 10.1016/j.geotexmem.2015.07.006.

Mousavi, S. Hamed, Mohammed A. Gabr, and Roy H. Borden. 2017. "Optimum Location of Geogrid Reinforcement in Unpaved Road." *Canadian Geotechnical Journal* 54(7):1047–54. doi: 10.1139/cgj-2016-0562.

Newland, P. L., and B. H. Allely. 1959. "Volume Changes During Undrained Triaxial Tests on Saturated Dilatant Granular Materials." *Géotechnique* 9(4):174–82. doi: 10.1680/geot.1959.9.4.174.

Ngo, Ngoc Trung, Buddhima Indraratna, and Cholachat Rujikiatkamjorn. 2017. "A Study of the Geogrid–Subballast Interface via Experimental Evaluation and Discrete Element Modelling." *Granular Matter* 19(3):54. doi: 10.1007/s10035-017-0743-4.

O'Connor, Ruaidhrí Manfried. 1996. "A Distributed Discrete Element Modeling Environment Algorithms, Implementation and Applications." Ph.D. Thesis, Massachusetts Institute of Technology.

Ostoja-Starzewski, Martin. 2002. "Lattice Models in Micromechanics." *Applied Mechanics Reviews* 55(1):35–60. doi: 10.1115/1.1432990.

Palmeira, Ennio Marques. 2009. "Soil–Geosynthetic Interaction: Modelling and Analysis." *Geotextiles and Geomembranes* 27(5):368–90. doi: 10.1016/j.geotexmem.2009.03.003.

Palmeria, E. M., and G. W. E. Milligan. 1989. "Scale and Other Factors Affecting the Results of Pull-out Tests of Grids Buried in Sand." *Géotechnique* 39(3):511–42. doi: 10.1680/geot.1989.39.3.511.

Perkins, S. W., and M. Q. Edens. 2003. "Finite Element Modeling of a Geosynthetic Pullout Test." *Geotechnical and Geological Engineering* 21(4):357–75. doi: 10.1023/B:GEGE.0000006053.77489.c5.

Pham, Thang Quyet. 2009. "Investigating Composite Behavior of Geosynthetic-Reinforced Soil (GRS) Mass." Ph.D. Thesis, University of Colorado Denver.

Pham, Thang, M. W. Zaman, and Thuy Vu. 2020. "Modeling Triaxial Testing with Flexible Membrane to Investigate Effects of Particle Size on Strength and Strain Properties of Cohesionless Soil." *Transportation Infrastructure Geotechnology* Under review.

Potyondy, D. O., and P. A. Cundall. 2004. “A Bonded-Particle Model for Rock.” *International Journal of Rock Mechanics and Mining Sciences* 41(8):1329–64. doi: 10.1016/j.ijrmms.2004.09.011.

Powrie, W., Q. Ni, R. M. Harkness, and X. Zhang. 2005. “Numerical Modelling of Plane Strain Tests on Sands Using a Particulate Approach.” *Géotechnique* 55(4):297–306. doi: 10.1680/geot.2005.55.4.297.

Qian, Yu, Debakanta Mishra, Erol Tutumluer, and Hasan A. Kazmee. 2015. “Characterization of Geogrid Reinforced Ballast Behavior at Different Levels of Degradation through Triaxial Shear Strength Test and Discrete Element Modeling.” *Geotextiles and Geomembranes* 43(5):393–402. doi: 10.1016/j.geotexmem.2015.04.012.

Qu, Tongming, Y. T. Feng, Yong Wang, and Min Wang. 2019. “Discrete Element Modelling of Flexible Membrane Boundaries for Triaxial Tests.” *Computers and Geotechnics* 115:103154. doi: 10.1016/j.compgeo.2019.103154.

Raymond, Gerald, and Issa Ismail. 2003. “The Effect of Geogrid Reinforcement on Unbound Aggregates.” *Geotextiles and Geomembranes* 21(6):355–80. doi: 10.1016/S0266-1144(03)00044-X.

Rowe, P. W. 1962. “The Stress-Dilatancy Relation for Static Equilibrium of an Assembly of Particles in Contact.” *Proceedings of the Royal Society of London. Series A. Mathematical and Physical Sciences* 269(1339):500–527. doi: 10.1098/rspa.1962.0193.

Rowe, R. Kerry, and S. K. Ho. 1998. “Horizontal Deformation in Reinforced Soil Walls.” *Canadian Geotechnical Journal* 35(2):312–27. doi: 10.1139/t97-062.

Rowe, R. Kerry, and K. W. Liu. 2015. “Three-Dimensional Finite Element Modelling of a Full-Scale Geosynthetic-Reinforced, Pile-Supported Embankment.” *Canadian Geotechnical Journal* 52(12):2041–54. doi: 10.1139/cgj-2014-0506.

Sadat Taghavi, S. H., and M. Mosallanezhad. 2017. “Experimental Analysis of Large-Scale Pullout Tests Conducted on Polyester Anchored Geogrid Reinforcement Systems.” *Canadian Geotechnical Journal* 54(5):621–30. doi: 10.1139/cgj-2016-0365.

Saha Roy, S., and K. Deb. 2017. “Effects of Aspect Ratio of Footings on Bearing Capacity for Geogrid-Reinforced Sand over Soft Soil.” *Geosynthetics International* 24(4):362–82. doi: 10.1680/jgein.17.00008.

Saussus, D. R., and J. D. Frost. 2000. “Simulating the Membrane Contact Patterns of Triaxial Sand Specimens.” *International Journal for Numerical and Analytical Methods in Geomechanics* 24(12):931–46. doi: 10.1002/1096-9853(200010)24:12<931::AID-NAG100>3.0.CO;2-4.

Seo, Min-Woo, Ik-Soo Ha, and Bum-Joo Kim. 2007. “Effects of Particle Size and Test Equipments on Shear Behavior of Coarse Materials.” *Journal of The Korean Society of Civil Engineers* 27(6C):393–400.

Shen, Wei-Gang, Tao Zhao, Giovanni Battista Crosta, and Feng Dai. 2017. "Analysis of Impact-Induced Rock Fragmentation Using a Discrete Element Approach." *International Journal of Rock Mechanics and Mining Sciences* 98:33–38. doi: 10.1016/j.ijrmms.2017.07.014.

Shin, E. C., and B. M. Das. 2000. "Experimental Study of Bearing Capacity of a Strip Foundation on Geogrid-Reinforced Sand." *Geosynthetics International* 7(1):59–71. doi: 10.1680/gein.7.0166.

Sitharam, T. G., and M. S. Nimbkar. 2000. "Micromechanical Modelling of Granular Materials: Effect of Particle Size and Gradation." *Geotechnical and Geological Engineering* 18(2):91–117. doi: 10.1023/A:1008982027109.

Sitharam, T. G., and S. Sireesh. 2004. "Model Studies of Embedded Circular Footing on Geogrid-Reinforced Sand Beds." *Proceedings of the Institution of Civil Engineers - Ground Improvement* 8(2):69–75. doi: 10.1680/grim.2004.8.2.69.

Sitharam, Thallak. G., S. V. Dinesh, and N. Shimizu. 2002. "Micromechanical Modelling of Monotonic Drained and Undrained Shear Behaviour of Granular Media Using Three-Dimensional DEM." *International Journal for Numerical and Analytical Methods in Geomechanics* 26(12):1167–89. doi: 10.1002/nag.240.

Skejic, Adis, Senad Medic, and Samir Dolarevic. 2018. "Influence of Wire Mesh Characteristics on Reinforced Soil Model Wall Failure Mechanisms-Physical and Numerical Modelling." *Geotextiles and Geomembranes* 46(6):726–38. doi: 10.1016/j.geotexmem.2018.07.004.

Song, Fei, Huabei Liu, Liqiu Ma, and Hongbing Hu. 2018. "Numerical Analysis of Geocell-Reinforced Retaining Wall Failure Modes." *Geotextiles and Geomembranes* 46(3):284–96. doi: 10.1016/j.geotexmem.2018.01.004.

Stahl, M., and L. te Kamp. 2013. *Project 13008: Geogrid Modelling with PFC3D — Generation and Calibration of Biaxial Geogrid SS20*. 01–2013. Itasca Consultants GmbH, Gelsenkirchen, Germany: Tensar International Ltd.

Stahl, Michael, and Heinz Konietzky. 2011. "Discrete Element Simulation of Ballast and Gravel under Special Consideration of Grain-Shape, Grain-Size and Relative Density." *Granular Matter* 13(4):417–28. doi: 10.1007/s10035-010-0239-y.

Stahl, Michael, Heinz Konietzky, Lothar te Kamp, and Hein Jas. 2014. "Discrete Element Simulation of Geogrid-Stabilised Soil." *Acta Geotechnica* 9(6):1073–84. doi: 10.1007/s11440-013-0265-0.

Tavakoli Mehrjardi, Gh., A. Ghanbari, and H. Mehdizadeh. 2016. "Experimental Study on the Behaviour of Geogrid-Reinforced Slopes with Respect to Aggregate Size." *Geotextiles and Geomembranes* 44(6):862–71. doi: 10.1016/j.geotexmem.2016.06.006.

Tran, V. D. H., M. A. Meguid, and L. E. Chouinard. 2013. "A Finite–Discrete Element Framework for the 3D Modeling of Geogrid–Soil Interaction under Pullout Loading

Conditions." *Geotextiles and Geomembranes* 37:1–9. doi: 10.1016/j.geotexmem.2013.01.003.

Vermeer, P. A. 1990. "The Orientation of Shear Bands in Biaxial Tests." *Géotechnique* 40(2):223–36. doi: 10.1680/geot.1990.40.2.223.

Wang, Jianfeng, and Haibin Yan. 2013. "On the Role of Particle Breakage in the Shear Failure Behavior of Granular Soils by DEM: ROLE OF PARTICLE BREAKAGE IN SHEAR FAILURE OF SOILS." *International Journal for Numerical and Analytical Methods in Geomechanics* 37(8):832–54. doi: 10.1002/nag.1124.

Wang Yuannian, and Tonon Fulvio. 2009. "Modeling Triaxial Test on Intact Rock Using Discrete Element Method with Membrane Boundary." *Journal of Engineering Mechanics* 135(9):1029–37. doi: 10.1061/(ASCE)EM.1943-7889.0000017.

Wang, Zhijie, Felix Jacobs, and Martin Ziegler. 2014. "Visualization of Load Transfer Behaviour between Geogrid and Sand Using PFC2D." *Geotextiles and Geomembranes* 42(2):83–90. doi: 10.1016/j.geotexmem.2014.01.001.

Wang, Zhijie, Felix Jacobs, and Martin Ziegler. 2016. "Experimental and DEM Investigation of Geogrid–Soil Interaction under Pullout Loads." *Geotextiles and Geomembranes* 44(3):230–46. doi: 10.1016/j.geotexmem.2015.11.001.

Wilson, José Francisco, and Esteban Sáez. 2017. "Use of Discrete Element Modeling to Study the Stress and Strain Distribution in Cyclic Torsional Shear Tests." *Acta Geotechnica* 12(3):511–26. doi: 10.1007/s11440-017-0526-4.

Xiao, Chengzhi, Jie Han, and Zhen Zhang. 2016. "Experimental Study on Performance of Geosynthetic-Reinforced Soil Model Walls on Rigid Foundations Subjected to Static Footing Loading." *Geotextiles and Geomembranes* 44(1):81–94. doi: 10.1016/j.geotexmem.2015.06.001.

Xiaofeng, X. U., W. E. I. Houzhen, Meng Qingshan, W. E. I. Changfu, and L. I. Yonghe. 2013. "DEM SIMULATION ON EFFECT OF COARSE GRAVEL CONTENT TO DIRECT SHEAR STRENGTH AND DEFORMATION CHARACTERISTICS OF COARSE-GRAINED SOIL." 工程地质学报 21(2):311–16.

Xie, Yongli, and Xiaohua Yang. 2009. "Characteristics of a New-Type Geocell Flexible Retaining Wall." *Journal of Materials in Civil Engineering* 21(4):171–75. doi: 10.1061/(ASCE)0899-1561(2009)21:4(171).

Xu, Chao, Cheng Liang, and Panpan Shen. 2019. "Experimental and Theoretical Studies on the Ultimate Bearing Capacity of Geogrid-Reinforced Sand." *Geotextiles and Geomembranes* 47(3):417–28. doi: 10.1016/j.geotexmem.2019.01.003.

Xu, Chao, Cheng Liang, Panpan Shen, and Fei Chai. 2020. "Experimental and Numerical Studies on the Reinforcing Mechanisms of Geosynthetic-Reinforced Granular Soil under

a Plane Strain Condition." *Soils and Foundations* 60(2):466–77. doi: 10.1016/j.sandf.2020.03.003.

Xue, Jian-Feng, Jian-Feng Chen, Jun-Xiu Liu, and Zhen-Ming Shi. 2014. "Instability of a Geogrid Reinforced Soil Wall on Thick Soft Shanghai Clay with Prefabricated Vertical Drains: A Case Study." *Geotextiles and Geomembranes* 42(4):302–11. doi: 10.1016/j.geotexmem.2014.05.003.

Yogarajah, I., and K. C. Yeo. 1994. "Finite Element Modelling of Pull-out Tests with Load and Strain Measurements." *Geotextiles and Geomembranes* 13(1):43–54. doi: 10.1016/0266-1144(94)90056-6.

Zhang, Zelin, Tao Wang, Shuren Wu, Huiming Tang, and Changyu Liang. 2017. "Seismic Performance of Loess-Mudstone Slope in Tianshui – Centrifuge Model Tests and Numerical Analysis." *Engineering Geology* 222:225–35. doi: 10.1016/j.enggeo.2017.04.006.

Zhao Xueliang, and Evans T. Matthew. 2009. "Discrete Simulations of Laboratory Loading Conditions." *International Journal of Geomechanics* 9(4):169–78. doi: 10.1061/(ASCE)1532-3641(2009)9:4(169).

Zhou, J., J. F. Chen, J. F. Xue, and J. Q. Wang. 2012. "Micro-Mechanism of the Interaction between Sand and Geogrid Transverse Ribs." *Geosynthetics International* 19(6):426–37. doi: 10.1680/gein.12.00028.

Zhuang, Y., and K. Y. Wang. 2016. "Finite-Element Analysis on the Effect of Subsoil in Reinforced Piled Embankments and Comparison with Theoretical Method Predictions." *International Journal of Geomechanics* 16(5):04016011. doi: 10.1061/(ASCE)GM.1943-5622.0000628.

APPENDIX

APPENDIX A

Please follow this link to download the PFC code:

https://drive.google.com/drive/folders/1q2SCNKasiP7EDCs7CVqityOy6lxULJCc?usp=sharing

BIOGRAPHICAL SKETCH

Md. Wasif Zaman was born on July 5, 1994, in Dhaka, Bangladesh. He attended Islamic University of Technology in Bangladesh and received a Bachelor of Science in Civil Engineering degree in 2016. He served as a lecturer in a university in Bangladesh prior to starting his master's study. Md. Wasif received his Master of Science in Civil Engineering from University of Texas Rio Grande Valley in December 2020. Md. Wasif is married to Asma Akter Moushumi who has a degree in Bachelor of Business Administration. Md. Wasif is preparing himself to start Ph.D. study at the University of Kansas beginning from Spring 2021. His career objective is to continue employment in the academia. Permanent Mailing Address, House: 29/31, Road: 18, Sector: 7, Uttara Model Town, Dhaka 1230, Bangladesh.